

# **Hybrid Energy Storage System for DC Nano-grids**

Zaid Hamed Zaid

A Thesis

In the Department

Of

Electrical and Computer Engineering

Presented in Partial Fulfillment of the Requirements

For the Degree of

Master of Science (Electrical and Computer Engineering) at

Concordia University

Montréal, Québec, Canada

February 2019

© Zaid Hamed Zaid, 2019

**CONCORDIA UNIVERSITY**  
**SCHOOL OF GRADUATE STUDIES**

This is to certify that the thesis prepared

By: **Zaid Zaid**

Entitled: **Hybrid Energy Storage System for DC Nano-grids**

and submitted in partial fulfillment of the requirements for the degree of

**Master of Applied Science**

Complies with the regulations of this University and meets the accepted standards with respect to originality and quality.

Signed by the final examining committee:

_____	Chair
Dr. Shahin Hashtrudi Zad	
_____	Examiner, External
Dr. Walter Lucia (CIISE)	To the Program
_____	Examiner
Dr. Shahin Hashtrudi Zad	
_____	Supervisor
Dr. Luiz Antonio C. Lopes	
_____	Co-Supervisor
Dr.	

Approved by: \_\_\_\_\_

Dr. W. E. Lynch, Chair

Department of Electrical and Computer Engineering

\_\_\_\_\_ 2019 \_\_\_\_\_

Dr. Amir Asif, Dean

Gina Cody School of Engineering and  
Computer Science

## Abstract

### **Hybrid Energy Storage System for DC Nano-grids**

Zaid Hamed Zaid

Solar photovoltaic (PV) panels and wind turbines are two commonly employed Renewable Energy Sources (RESs). Their main drawback is that they are stochastic and fluctuating sources. Roof-top PV is easier to install and operate in the urban environment. Due to the variable nature of RESs, an energy storage system (ESS) is used to solve the problem of mismatches between the variable power generation and load demand in standalone/islanded systems. The ESS is employed to store surplus energy and supply it back to the system when needed. The most common ESS applied in standalone PV systems is based on batteries. Batteries, in general, have high energy density but low power density, giving low charge/discharge rates. Based on the characteristics of the batteries, it will not be able to respond optimally to fast changing and high frequency power exchanges. One solution to this limitation is by combining batteries and supercapacitors (SCs), which can provide high power but have low energy storage capacity, to form a hybrid ESS (HESS). A battery-SC combination has been considered in this Thesis. The aim of this combination is to reduce the current stresses on the battery occurring due to sudden changes in PV generating and load demand. For that, an effective control method is essential for the optimal operation of the HESS with varying load demand and PV generation.

This Thesis discusses a control strategy for a HESS consisting of three proportional plus integral (PI) type controllers that control the currents of two bidirectional power electronic converters, one for the battery and the other for the SC, connecting them to a common DC bus, whose voltage should be regulated. The boost mode has been considered for modeling the class C interface power converters and designing the relevant PI controllers. For the sake of determining the reference currents for both converters, a low pass filter is used to split the HESS current, required to regulate the common DC bus voltage, into low dynamic components for the battery and fast dynamic components for the SC. First, the analysis of the ESS with a single element (battery) is used with

the PV system and variable load to test the performance of the basic inner current and outer DC nano-grid voltage regulation loop. Later, the battery and SC units are used along with the PV system to verify whether the current split technique, with fast dynamic to the SC, can provide fast regulation of the DC bus voltage while reducing the current stress on the battery. A SC voltage control loop has also been designed to keep the SC voltage with a certain reference value. DC nano-grids can also be connected to an AC utility grid. This is usually done by means of a single-phase DC-AC converter that tends to produce a low order voltage harmonic in the DC bus. The usual solution based on a large electrolytic capacitor, presents the drawback that this component presents a short lifetime. The solution employed in this work was to use the HESS to perform an active filtering function, what was accomplished by adding a resonant (R) term to the PI of the DC bus voltage loop. The effectiveness of the control scheme is shown by simulation studies in MATLAB®/Simulink. Finally, experimental results are provided to verify those described by theoretical analysis as well as simulation results.

I dedicate this work to my brother, who has passed away during my studies...

## ACKNOWLEDGMENTS

All praise and thanks go to Lord, the Most Merciful, the Most beneficent and the Most Giving, Creator ﷻ Allah.

I am heartily thankful to my supervisor, Dr. Luiz Lopes, for his encouragement, guidance and support from the initial to the final stage of my project. I am grateful to the University of Concordia for giving me the opportunity to achieve my academic goals. I owe my deep gratitude to the defense committee.

I would like also to thank all of those who taught me throughout my journey of my project. I am indebted to many of my colleagues and friends to support me during the completion of this project. A very special thanks to my colleagues and friend, Saroosh Saeed, Ahmed Malkawi, Khalid Elamari, Mahmoud Swessi, and my colleagues in the Power Electronics and Energy Research (PEER) group for their motivation and encouragement during my study.

Finally, I want to express my deepest gratitude to my brother, who has passed away during my studies. Last but not least, my deepest appreciation goes to my beloved family, my father, mother, brothers, sisters, and fiancée for their love, encouragement, and support.

# Contents

Abstract .....	iii
List of Figures .....	ix
List of Tables .....	xi
Nomenclature .....	xii
Chapter 1. Introduction .....	1
1.1 Scope and contribution of thesis .....	4
1.2 Thesis outline .....	4
Chapter 2. Hybrid Energy Storage System (HESS).....	5
2.1 Introduction.....	5
2.2 Configuration of the DC nano-grid.....	5
2.3 The control strategy for the HESS .....	6
2.4 Operating principle and specifications of the control strategy for the HESS .....	7
2.4.1 Calculating the plant transfer functions .....	8
2.4.2 Inner current control loop of the supercapacitor (SC).....	9
2.4.3 Inner current control loop of the battery.....	13
2.4.4 Design of the DC bus voltage control loop.....	15
2.5 Analysis of the operation of the PI controller for different operating conditions .....	18
2.6 Simulation results.....	19
2.7 Conclusion .....	23
Chapter 3. Improving the Control Strategy of the HESS.....	24
3.1 Selecting the LPF/HPF (frequency) of the HESS (SC + Batt).....	24
3.1.1 Analysis of the HPF (frequency) on the splitting of the HESS reference current.....	24
3.1.2 Simulation results.....	29
3.2 A voltage control loop for the SC .....	32
3.2.1 Design of the voltage control loop for the SC.....	33
3.2.2 Simulation results.....	35
3.3 A voltage control loop to compensate the low order harmonics of the grid interface. ....	37
3.3.1 Design of a voltage control loop to compensate the low order harmonics in the DC nano-grid. ....	39
3.3.2 Simulation results.....	41
3.4 Conclusion .....	47
Chapter 4. Experimental Implementation .....	48

4.1	Experimental setup.....	48
4.2	Experimental results.....	51
4.2.1	Results of the PI controller at different operating conditions .....	51
4.2.2	Results concerning the choice of the HPF (frequency) of a HESS.....	55
4.3	Conclusion .....	57
Chapter 5.	Conclusions and Future Work.....	58
References.....		60

## List of Figures

Figure 1.1: A grid connected DC nano-grid .....	3
Figure 2.1: Typical configuration of a stand-alone PV-based DC nano-grid [1].....	6
Figure 2.2: Control scheme.....	7
Figure 2.3: Boost converter with the load.....	8
Figure 2.4: Bode plot of the plant for the design of the current loop of the SC.....	11
Figure 2.5: Bode plot of the plant $Gp_{is}$ , and the LTF of the SC .....	12
Figure 2.6: Bode plot of the plant for the design of the battery current loop.....	14
Figure 2.7: Bode plot of the current loop of the battery.....	15
Figure 2.8: Bode plot of the plant .....	16
Figure 2.9: Bode plot of the voltage control loop of the HESS .....	17
Figure 2.10: Bode plot of the plant $Gp_v$ , and the LTF of the voltage loop.....	18
Figure 2.11: Bode plot of the plant $Gp_v$ , and the LTF of the voltage loop.....	19
Figure 2.12: Waveforms for the system with a step load variation (6 to 9 $\Omega$ ): a) DC bus voltage; b) Battery current; c) SC current; d) SC voltage .....	20
Figure 2.13: Waveforms for the system with a step load variation (6 to 9 $\Omega$ ): a) DC bus voltage; b) Battery current; c) SC current; d) SC voltage. ....	21
Figure 2.14: Waveforms for the system with a step load variation (6 to 9 $\Omega$ ):a)DC bus voltage; b) Battery current; c) SC current ;d)SC voltage.....	22
Figure 3.1: Block diagram of the system .....	25
Figure 3.2: Block diagram of the equivalent system.....	26
Figure 3.3: Step responses of the $I_{sc}Idiss$ and $I_{HES}Idiss$ with different values of the cut-off frequency of the HPF .....	28
Figure 3.4: Step responses of the $I_{sc}Idiss$ and $I_{HES}Idiss$ with cut-off frequency of HPF $f = 0.37$ Hz. ....	29
Figure 3.5: Waveforms for the system with $f = 0.37$ Hz for a step load variation (9 to 6 $\Omega$ ) applied at $t = 3$ s: a) SC current; b) Battery current; c) DC bus voltage; d) Energy supplied by the SC. ....	30
Figure 3.6: Waveforms for the system with $f = 0.037$ Hz for a step load variation (9 to 6 $\Omega$ ) applied at $t = 3$ s: a) SC current; b) Battery current; c) DC bus voltage; d) Energy supplied by the SC.. ....	31
Figure 3.7: Waveforms for the system with $f = 0.0037$ Hz for a step load variation (9 to 6 $\Omega$ ) applied at $t = 3$ s: a) SC current; b) Battery current; c) DC bus voltage; d) Energy supplied by the SC. ....	32
Figure 3.8: Block diagram of the SC voltage control loop. ....	33
Figure 3.9: Control scheme of the HESS.....	35

Figure 3.10: Waveforms for the system without voltage control for SC: a) DC bus voltage; b) Battery current; c) SC current; d) SC voltage.....	36
Figure 3.11: Waveforms for the system without voltage control for SC: a) DC bus voltage; b) Battery current; c) The actual SC current; d) SC voltage; e) The two reference currents of the SC. ....	37
Figure 3.12: PV system with a single-phase dc/ac converter [8]. ....	38
Figure 3.13: Frequency responses of a non-ideal PI+R controller when $K_i'$ changes. ....	40
Figure 3.14: Frequency responses of a non-ideal PI+R controller when $\omega_c$ changes. ....	41
Figure 3.15: PV system and HESS with a single-phase dc/ac converter. ....	42
Figure 3.16: Control scheme of the HESS. ....	42
Figure 3.17: Waveforms for the system with PI Control: a) DC bus voltage; b) Battery current; c) SC current. ....	43
Figure 3.18: Waveforms for the system with PI+R Control: a) DC bus voltage; b) Battery current; c) SC current. ....	44
Figure 3.19: Waveforms for the system with PI+R Control: a) DC bus voltage; b) Battery current; c) SC current. ....	45
Figure 3.20: Waveforms for the system with PI Control: a) DC bus voltage; b) Battery current; c) SC current. ....	46
Figure 4.1: DC nano-grid power electronics interfaces. ....	49
Figure 4.2: Picture of the experimental set-up assembled in the laboratory. ....	50
Figure 4.3: Waveforms for the system with a step load variation (9 to 6 $\Omega$ ): a) SC current; b) Battery current; c) Load current; d) DC bus voltage .....	52
Figure 4.4: Waveforms for the system with a step load variation (9 to 6 $\Omega$ ): a) SC current; b) Battery current; c) Load current; d) DC bus voltage .....	53
Figure 4.5: Waveforms for the system with a step load variation (9 to 6 $\Omega$ ) :a) SC current; b) Battery current; c)Load current; d) DC bus voltage .....	54
Figure 4.6: Waveforms for the system with $f = 0.37\text{Hz}$ for a step load variation (20 to 13 $\Omega$ ): a) SC current; b) Battery current; c) Load current; d) DC bus voltage. ....	55
Figure 4.7: Waveforms for the system with $f = 0.037\text{Hz}$ for a step load variation (20 to 13 $\Omega$ ):a) SC current; b) Battery current; c) Load current; d) DC bus voltage. ....	56
Figure 4.8: Waveforms for the system with $f = 0.0037\text{Hz}$ for a step load variation (20 to 13 $\Omega$ ): a) SC current; b) Battery current; c) Load current; d) DC bus voltage. ....	57

## List of Tables

Table 2.1: Nominal SC converter parameters .....	10
Table 2.2: Nominal battery converter parameters.....	13
Table 3.1: Time of contribution of the SC and cut-off frequency of the HPF.....	27
Table 4.1: Parameter of the PI controller for the SC voltage control loop. ....	34

## Nomenclature

RAPS: Remote Area Power System.

ESS: Energy Storage System.

RES: Renewable Energy Source.

HESS: Hybrid Energy Storage System.

NZEH: Net-zero Energy Home.

EV: Electric Vehicle.

PV: Photovoltaic.

BESS: Battery Energy Storage System.

MPPT: Maximum power point tracking.

LPF: Low Pass Filter.

HPF: High Pass Filter.

SC: Supercapacitor.

PI: Proportional-integral.

PM: Phase Margin.

PWM: Pulse width modulator.

BW: Bandwidth.

D: Duty Cycle.

LTF: Loop Transfer Function.

SAS: Solar Array Simulator.

## Chapter 1. Introduction

Hybrid energy storage systems (HESSs) are implemented to support a power system by actively supplying or absorbing electric power as well as to have effective and optimal utilization of different energy storage elements. The basic idea of an HESS is to combine batteries and supercapacitors to achieve a better overall performance. This combination inherently offers better performance in comparison to the use of either of them alone. HESSs can improve the performance of several applications. They are particularly suitable for stationary applications such as residential nano-grids and micro-grids and for transport system such as EVs, trains..etc.

This combination can effectively solve the issue of varying power and energy fluctuations in a number of applications. For that, an effective control method is essential for the optimal operation of the HESS with varying load demand. In order to control the average and dynamic power sharing between the Battery and the Supercapacitor, there are different control strategies that have been reported in literature [1]-[29]. These control strategies include fuzzy logic control, neural networks and model predictive control (MPC). *El Fadil et al.* [29] presented a nonlinear controller technique for tight dc voltage regulation and effective SC current tracking for electrical vehicles (EVs) with fuel cell and SC. In [28], MPC is implemented to control the HESS currents and to maintain the state-of-charge (SOC) of the battery and the SC within predefined limits. However, the drawbacks of the proposed method are dependence on the discrete model of the system and cost function. It also uses a quadratic programming solver to calculate the optimal control, with significant computational time. *Dusmez and Khaligh* [27] proposed the wavelet-based frequency decoupling technique for HESS control in EV application. However, the aforesaid control strategy requires larger computational times and resources. In [25], a multimode fuzzy logic based HESS controller for PV system was designed and demonstrated the increased battery life. In [19], it is shown that the battery lifetime can be enhanced up to four times when it is operated in combination with a SC. A decentralized control strategy for dynamic power sharing between the HESS is presented in [17]. The proposed method is based on the virtual resistance and capacitance droop coefficients. The droop coefficient inherently acts as a low-pass filter (LPF) for the battery and high-pass filter for the SC during generation and load variation. However, the above mentioned control strategies have drawbacks that they require larger computational times and resources. The basic idea behind the above mentioned controller is that the batteries support the temporary slow power fluctuations

while the supercapacitors support the high frequency power fluctuations. *Kollimalla, Mishra, and Narasamma* proposed a control strategy for dynamic power sharing between the HESS as presented in [1]. The proposed control strategy is simple to implement, effective and does not requires large computational time and resources. However, it does not discuss the sizing of the storage units and the expected sharing of the compensating currents among the SC and battery converters. Neither typical values of the cut-off frequency of the LPF, nor approaches for calculating it. While many design considerations have been addressed by researchers, most discussions focus on the specific topology used, with not much detail from the system perspective. This Thesis discusses the design considerations that should be considered in the development of battery and SC HESS topologies such as design approaches for calculating the cut-off frequency of the LPF as well as the design of the voltage control loop for the SC.

With increasing demand of energy, renewable energy sources are gaining popularity all over the world. Renewable energy sources can mitigate environmental issues of power generation. However, these sources are stochastic and fluctuating in nature. In order to provide back-up power when the available power from these sources is not sufficient to meet the load demand, various storage systems can be added to the system. Nano-grids provide an easier integration of renewable sources and storage units and can be based on AC or DC nano-grids distribution. The nano-grids can be operated either in stand-alone/islanded mode or connected to the AC utility system. For operation in stand-alone, the renewable energy sources such as PV and storage units should have enough power generation and storage capacity to supply the load demand. The system considered in this Thesis is a PV source supplying a DC bus with MPPT and having a hybrid energy storage system (HESS) to balance power supply and load demand thus regulating the DC bus voltage. In order to connect the battery and supercapacitor (SC) of the HESS with the PV system to supply power to a DC load, class C DC-DC converters are used for the interfaces. So, power flow can be controlled in both directions by controlling the current in the battery and supercapacitor.

In the grid-connected mode, the power generation can be less and depending on the load demand and amount of power generation, power flow can be from the nano-grid to the utility. A DC nano-grid is connected to an AC utility through interface converters, what is performed by a DC-AC converter or inverter. The single-phase DC-AC grid interface converter provides bidirectional power flow, but it draws/injects the expected DC component as well as an undesired AC current component, leading to a voltage ripple of twice the AC side fundamental frequency.

Usually, a large electrolytic capacitor is used to attenuate the voltage ripple in the DC bus voltage. However, this capacitor has a short life. *Dong et al.* [6] used a high-pass filter and feedback loop to suppress the 120 Hz common mode (CM) voltage ripple but it neglected the asymmetric DC bus voltage. In *Chen, Burgos, Boroyevich, and Xuning* [23], an active CM duty cycle injection method is proposed to reduce the low-frequency CM voltage ripple and generate symmetric dc-bus voltages. In *Burgos, and Dong* [10], the power stage is modeled and a bidirectional control system is designed. Besides the conventional PI compensator, a feedforward and a resonant controller are used to improve the ac grid side current waveform and to reduce the dc bus output voltage ripple with a "notch" filter tuned at the 120 Hz (2nd harmonic). In order for a smaller non-electrolytic capacitor to be used, some sort of active power filtering is needed. This can be done by means of the HESS with a suitable DC bus voltage control scheme as proposed in this Thesis. Therefore, the HESS control of [1] has been modified by adding a resonant element at the frequency of the disturbance to the PI controller of the DC bus voltage loop, making it a PI+R. With a high gain in the DC bus voltage loop at the frequency of the disturbance, it was possible to achieve a significant reduction in the 120 Hz voltage ripple of the DC nano-grid.

The DC nano-grid concept is appropriate for the realization of net-zero energy homes (NZEHS), a topic that is drawing lots of interest at this moment and that can also help mitigate the impact of Electric Vehicles (EVs) on the low voltage AC distribution system. A basic representation of a grid connected DC nano-grid is shown in Figure 1.1.

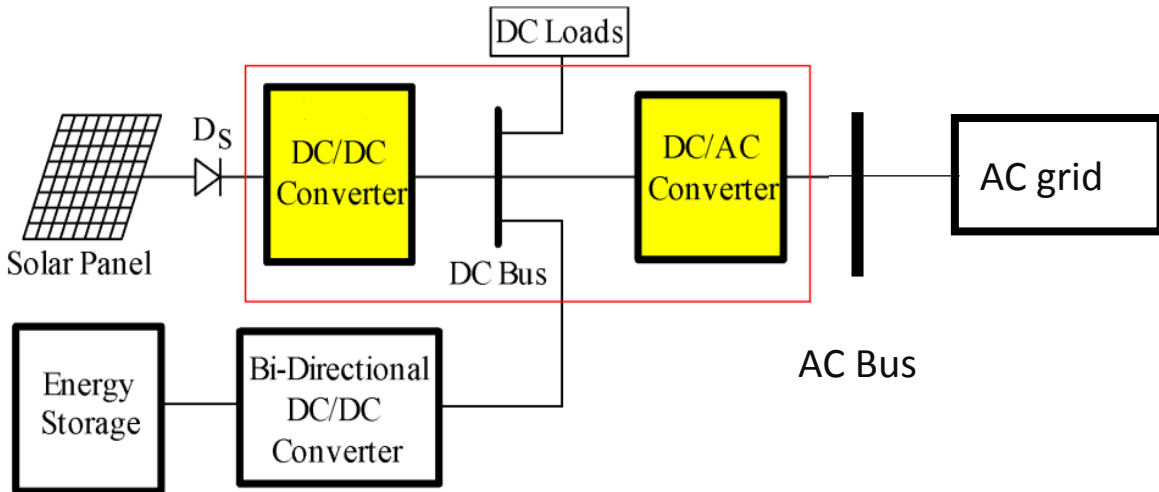


Figure 1.1: A grid connected DC nano-grid

## 1.1 Scope and contribution of thesis

This Thesis presents a control loop for the energy storage system of a DC nano-grid that takes into consideration the impact of the PV power and load demand variations, typical of autonomous DC systems, as well as that of AC grid-connected ones.

The main focus is on the design of a control strategy for a hybrid energy storage system (HESS) for various operating conditions for PV generation and load demand. Also, using bi-directional DC-DC converters for battery and supercapacitor to supply and absorb electric power depending on the operating conditions.

The main contributions of this Thesis are as follows

- 1) Design and testing of a multi-loop control strategy for a hybrid energy storage system (HESS).
- 2) Split, the dynamic current required from the HESS to regulate the DC bus voltage of the nano-grid between battery, slow, and SC, fast.
- 3) Selecting a suitable value of the current splitting HPF/LPF (frequency) of a hybrid energy storage system (SC + Bat), according to the duration of the SC current contribution, to regulate the DC bus voltage.
- 4) Design a DC bus voltage control loop to attenuate the 2nd order voltage ripple created by the single-phase DC-AC grid interface.
- 5) Verification of the system performance by means of simulation and experimental results

## 1.2 Thesis outline

The structure of this Thesis is as follows.

Chapter 2 discusses the control strategy of a hybrid energy storage system (HESS)

Chapter 3 presents and analyses the selection of the time constant of the HPF as well as the design of the voltage control loop to compensate low order harmonics in the DC nano-grid.

Chapter 4 presents an experimental implementation and results to validate the simulation results.

Chapter 5 presents the conclusion.

## Chapter 2. Hybrid Energy Storage System (HESS)

### 2.1 Introduction

An elementary PV system, may have a variable DC bus voltage due to variations in the amount of power supplied by the stochastic PV source and demanded by the variable load. An energy storage system (ESS) with a bidirectional converter can be used to compensate for unbalances in the energy supplied and absorbed in order to keep the voltage fixed across the DC bus. Batteries are commonly employed in ESSs, due to their high energy densities [1]. However, because of their relatively low power density, they should be controlled with low dynamic responses in order to limit their power losses and premature aging. This could result in a poor dynamic behavior for the voltage control loop. Conversely, supercapacitors have a high power density but a low energy density, making them not suitable for sole use in many ESSs [1], [2]. Therefore, an interesting approach is to combine both energy storage elements in a hybrid energy storage system (HESS). This increases the energy utilization over the battery life span as well as the dynamic regulation of the DC bus voltage.

### 2.2 Configuration of the DC nano-grid.

The basic system considered for this research work can be seen in Fig. 2.1 [1]. It consists of a PV panel, as a DC energy source, feeding a variable load  $R$ , through a DC-DC boost converter. This corresponds to the elementary PV system. The DC bus is also connected to the hybrid energy storage system (HESS) composed of a battery and a supercapacitor using conventional class C bidirectional dc/dc converters. For the class C bidirectional dc/dc converters to work, the voltage level at the storage side of the converter must be lower than that at the common DC bus voltage. Otherwise, the diodes in anti-parallel with  $Sw_1$  and  $Sw_4$  conduct and one loses control of the power/current flow. The class C converter can operate in two modes: Charging or step-down/buck, when the power flows from the common DC bus to the battery or SC, and discharging or step-up/boost mode, when the power flows from the battery or SC to the common DC bus. This allows both the battery and the supercapacitor to regulate the DC bus voltage. The main principle behind their action is that they will absorb power when the supply of PV power, assumed to be operating with maximum power point tracking (MPPT), exceeds the load demand what should make the

output voltage rise. Conversely, they will supply power when the PV cannot fully supply the total amount of power demanded by the load. The battery and the capacitor are connected to the main DC bus through power electronic interfaces that are controlled with multiple proportional-integral (PI) controllers, arranged in a cascaded scheme. A common configuration is with one outer voltage and individual inner current loops [1].

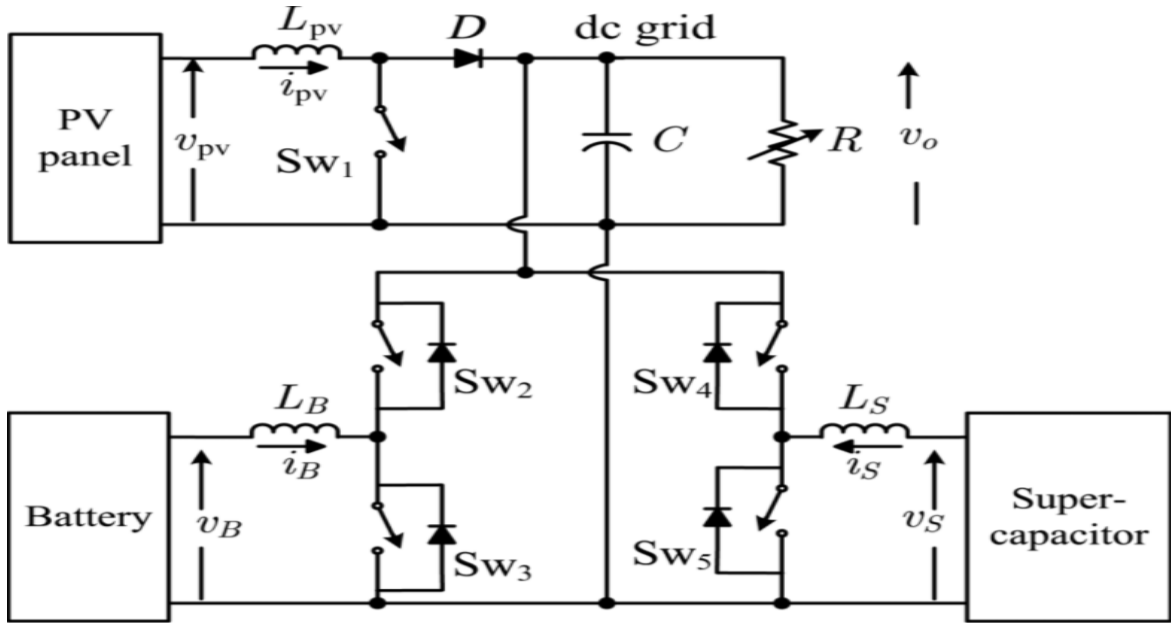


Figure 2.1: Typical configuration of a stand-alone PV-based DC nano-grid [1].

### 2.3 The control strategy for the HESS

The considered control circuit can be seen in Fig. 2.2 [1]. The DC bus voltage is compared to a desired reference value. The error is first fed to a PI controller that produces a reference current that will provide a suitable dynamic response and a zero DC bus voltage error in the steady-state. The reference current for the HESS, is then fed to a low pass filter (LPF) to split the low-frequency (slow changing) from the high frequency (fast changing) components. The output of the low pass filter is the battery reference current. Then, it is compared to the actual current of the battery and is fed to a PI controller that provides the modulating signal for the pulse width modulator (PWM) that defines the gating signals of the two switches of the battery converter. The output of the low pass filter is also subtracted from the total HESS reference current, the output of the PI controller

of the voltage loop. This is the reference current signal for the supercapacitor current. This is compared to the actual value and the error is fed to a PI controller that provides the modulating signal for the pulse width modulator (PWM) that defines the gating signals of the two switches of the supercapacitor converter.

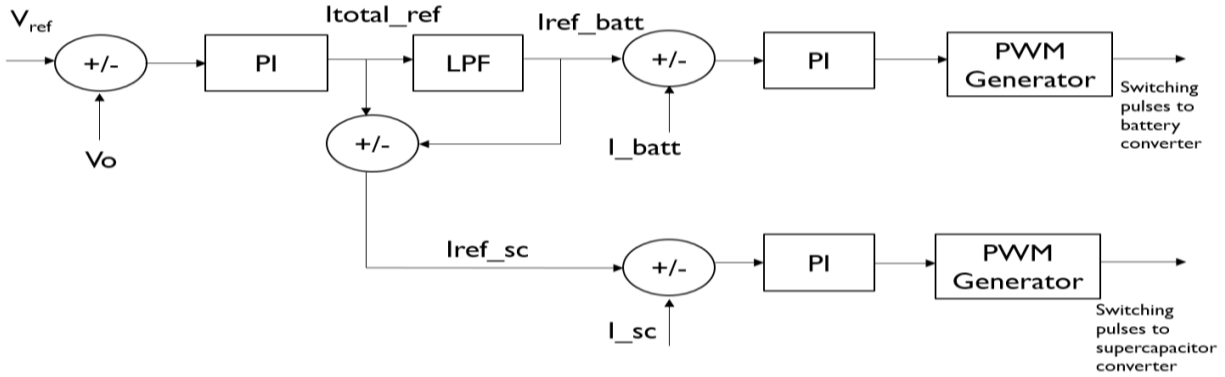


Figure 2.2: Control scheme.

#### 2.4 Operating principle and specifications of the control strategy for the HESS

It can be shown that a class C converter operating in the charging/buck and discharging/boost modes can be represented by the same  $I_L(s)/D(s)$  transfer function, where  $I_L$  is the inductor current and  $D$  is the duty cycle of the bottom switch of the class C converter. Therefore, a unified controller can be employed for both modes of operations. It should be noted that the switches of a class C converter operate complementarily and the signal of the PWM comparator is sent to the bottom switch of the converter. Three PI controllers will be designed to control the (inner) current through the supercapacitor and the battery as well as the outer DC bus voltage. The bandwidth of these controllers are chosen based on the speed of response of each single converter, which is a function of its switching frequency. The design of the inner current loops will be as a function of the duty cycle ( $D$ ), the control variable. From the characteristics of the SC, which has faster charge/discharge capabilities compared to the battery, the inner current loop bandwidth (BW) of the SC is  $\frac{f_{sw}}{6}$ , where  $f_{sw}$  is the switching frequency. The bandwidth of the (inner loop) battery current has to be lesser than the SC current loop BW. So, the BW of the battery current loop is chosen as  $\frac{f_{sw}}{10}$ . As usual in cascaded loops, the BW of the outer voltage loop is slower, 10%, than

the BW of the SC current loop [1]. The components of the reference currents of the supercapacitor and battery, low and high frequency respectively, will be determined later by the LPF.

#### 2.4.1 Calculating the plant transfer functions

The transfer function of the “plant” can be found based on the equations that describe the operation of the power electronics converter. From that, the PI controller for the current loops will be designed. The derivation of the plant model and the design steps of the controller are as follows:

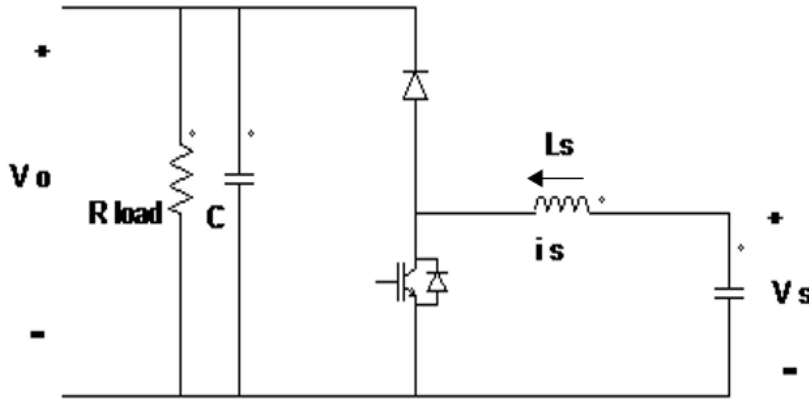


Figure2.3: Boost converter with the load.

- The operation of the class C DC-DC converter can be represented by two states

$$\text{ON state: } t_{on} = DT_s$$

$$\text{OFF state : } t_{off} = (1-D) T_s$$

$$l_s \frac{di_s}{dt} = V_s \quad (2-1)$$

$$l_s \frac{di_s}{dt} = V_s - V_o \quad (2-2)$$

$$c \frac{dV_o}{dt} = -\frac{V_o}{R} \quad (2-3)$$

$$c \frac{dV}{dt} = l_s - \frac{V_o}{R} \quad (2-4)$$

- Averaging the boost converter differential equations gives:

$$l_s \frac{di_s}{dt} = V_s - (1 - D)V_o \quad (2-5)$$

$$c \frac{dV_o}{dt} = (1 - D)l_s - \frac{V_o}{R} \quad (2-6)$$

- Introducing the small signal perturbations around a base operating point:

$$l_s \frac{d(\widetilde{i}_s + I_s)}{dt} = (V_s + \check{v}_s) - (1 - (D + \widetilde{d}))(V_o + \widetilde{v}_o) \quad (2-7)$$

$$c \frac{d(V_o + \widetilde{v}_o)}{dt} = (I_s + \check{i}_s)(1 - (D + \widetilde{d})) - \frac{(V_o + \widetilde{v}_o)}{R} \quad (2-8)$$

- The linearized equivalent model can be represented by

$$l_s \frac{d\widetilde{i}_s(t)}{dt} = \check{v}_s(t) - (1 - D)\widetilde{v}_o(t) + \widetilde{d}V_o \quad (2-9)$$

$$c \frac{d\widetilde{v}_o(t)}{dt} = \check{i}_s(t)(1 - D) - I_s\widetilde{d}(t) - \frac{\widetilde{v}_o(t)}{R} \quad (2-10)$$

- Using Laplace transform

$$L_s i_s(s) = v_s(s) - (1 - D)v_o(s) + d(s)V_o \quad (2-11)$$

$$Cv_o(s) = i_s(s)(1 - D) - I_s d(s) - \frac{v_o(s)}{R} \quad (2-12)$$

- Finding the transfer function of the plant for the design of the controller of the inductor current

$$G_{p_{is}}(s) = \frac{i_s(s)}{d(s)} = \frac{V_o C s + \frac{V_o}{R} + (1 - D)I_s}{C L_s s^2 + \frac{L_s}{R} s + (1 - D)^2} \quad (2-13)$$

#### 2.4.2 Inner current control loop of the supercapacitor (SC)

The bandwidth of the inner current loop of the SC is chosen by  $f_{xi} = \frac{f_{sw}}{6}$  and the switching frequency ( $f_{sw}$ ) considered in this work is 20 kHz. The crossover frequency is

becomes  $\omega_x = 2\pi f_{xi} = 20.93 \cdot 10^3 \text{ rad/sec}$  and the phase margin (PM) can be selected as  $60^\circ$ . Table 2.1 shows the basic parameters used for the operation of the supercapacitor interface.

Table 2.1: Nominal SC converter parameters

$V_S$	$I_S$	$V_O$	$L_S$	$D_S$	$R$	$C$
28.44V	2A	48V	100 $\mu$ H	0.4	40 $\Omega$	1500 $\mu$ F

The transfer function of the plant  $\frac{i_s(s)}{d(s)}$  becomes:

$$G_{p_{is}}(s) = \frac{i_s(s)}{d(s)} = \frac{0.072s + 2.4}{1.5e^{-7}s^2 + 2.5e^{-6}s + 0.4445} \quad (2-14)$$

At the crossover frequency one gets:

$$G_{p_{is}}(j\omega_x) = \frac{2.4 + j 1507.68}{-65.328 + j0.05235} \quad (2-15)$$

There, the gain and phase are computed as:

$$|G_{p_{is}}(j\omega_x)| = 27.26 \text{ dB} \quad \varphi_{p_{is}} = 89.93^\circ$$

Figure 2.4, illustrates the Bode plot of the transfer functions of the plant  $G_{p_{is}}(s)$

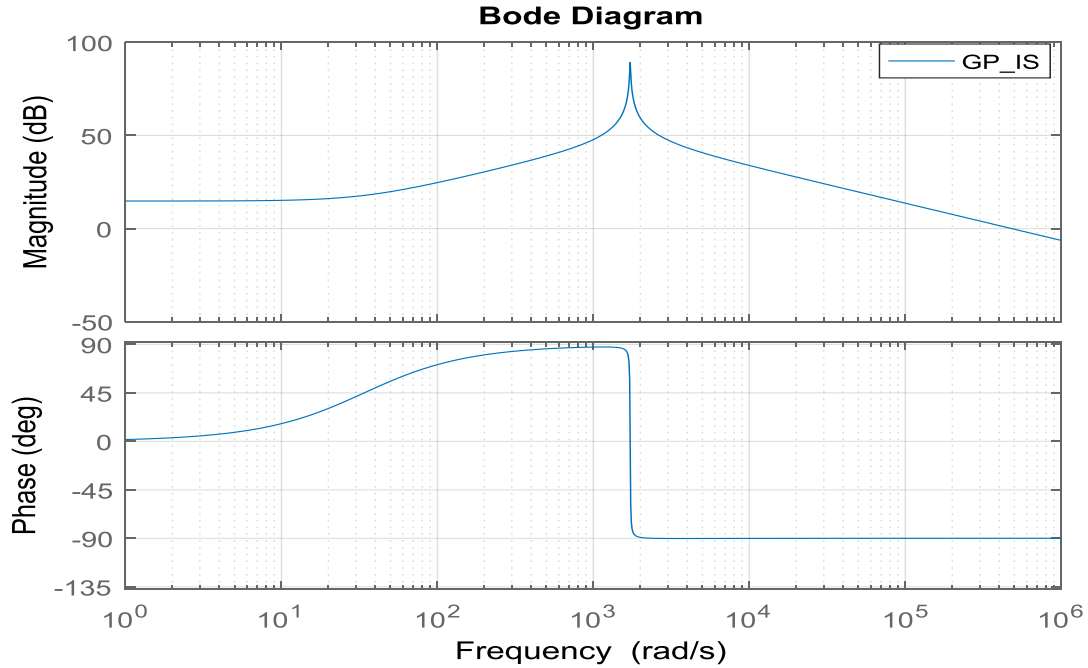


Figure 2.4: Bode plot of the plant for the design of the current loop of the SC.

In general, at the low frequency range, the loop gain should be high, to minimize the steady state error, and at the high frequency range, the gain should be low to limit/attenuate the switching harmonics. To obtain a satisfactory phase margin, the gain slope should be -20db/dec around the crossover frequency. As shown in Fig. 2.4 the Bode plot of the plant  $G_{p_{is}}$  presents a constant gain at the low frequency range. Therefore, an integrator is required to yield a negative slope (-20 dB/dec) and an infinite gain at DC (0 Hz).

The controller PI type II can be chosen for this plant and its transfer function is given by:

$$G_{pi_{is}}(s) = \frac{Ki(1 + s\tau)}{sT(1 + sTp)} \quad (2-16)$$

Calculating the boost angle at the crossover frequency using equations.

$$\varphi_c = -180^\circ + PM - \varphi_{p_{is}} \quad (2-17)$$

$$\varphi_{boost} = 90^\circ + \varphi_c \quad (2-18)$$

The other parameters may be easily obtained as follows in equations

$$K = \tan\left(\frac{\varphi_{boost}}{2} + 45\right) = 3.738 \quad (2-19)$$

$$\tau = \frac{k}{\omega_x} = 178.57 \mu\text{s} \quad (2-20)$$

$$T_p = \frac{1}{k\omega_x} = 12.77 \mu\text{s} \quad (2-21)$$

The gain of the PI type II controller “Ki” should be equal to the inverse of the plant’s gain at the crossover frequency  $\omega_x$ .

Therefore:

$$20 \log K_i = -27.26 \text{ dB} \quad (2-22)$$

$$K_i = 0.0433$$

Figure 2.5, illustrates the Bode plot of the transfer functions of the plant  $G_{pi\_is}$ , and the loop transfer function (LTF), with the designed controller. From there, one can see that the design specs ( $\omega_x = 2\pi f_x = 20.94 \cdot 10^3 \text{ rad/sec}$  and  $\text{PM} = 60^\circ$ ), where accomplished with the designed PI-type controller.

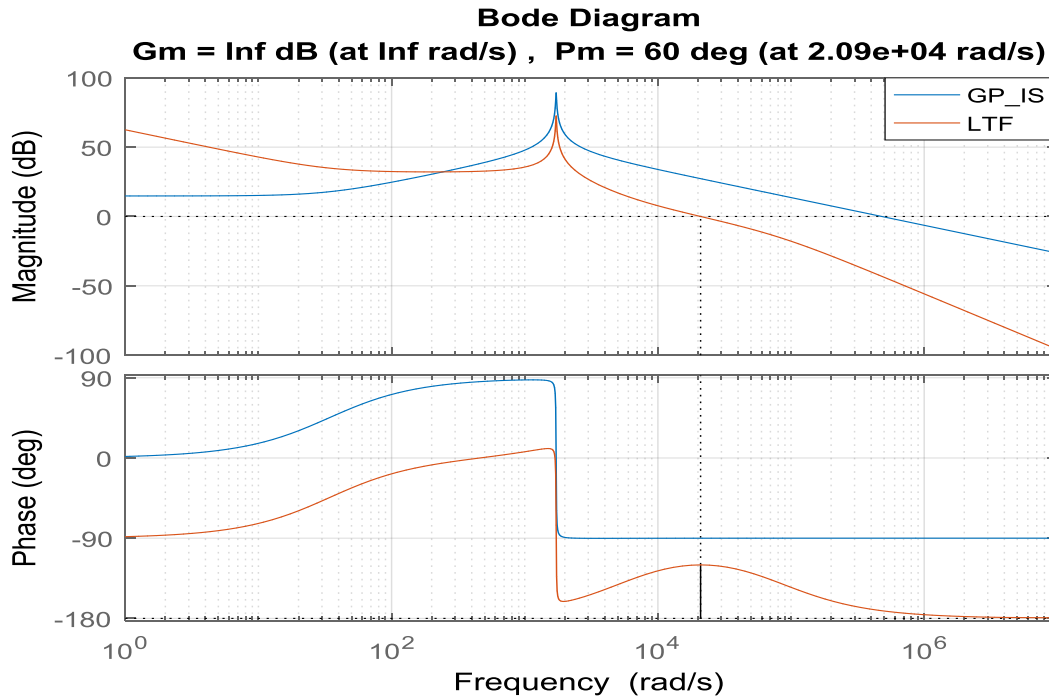


Figure 2.5: Bode plot of the plant  $G_{p\_is}$ , and the LTF of the SC

### 2.4.3 Inner current control loop of the battery.

By following the same steps, one can design the current controller of the battery converter. Like for the supercapacitor, the plant transfer function is given as

$$G_{p\_ib}(s) = \frac{i_B(s)}{d(s)} = \frac{V_o Cs + \frac{V_o}{R} + (1 - D)I_B}{CL_B s^2 + \frac{L_B}{R} s + (1 - D)^2} \quad (2-23)$$

Since the battery current is supposed to react at a slower pace than the supercapacitor current, one can select  $f_{xi} = \frac{f_{sw}}{10}$ , the crossover frequency is chosen by  $\omega_x = 2\pi f_{xi} = 12.56$  krad/s and the phase margin  $PM = 60^\circ$ . Table 2.2 shows the basic parameters used for the operation of the battery interface.

Table 2.2: Nominal battery converter parameters

$V_B$	$I_B$	$V_o$	$L_B$	$D_B$	$R$	$C$
24V	2.4A	48V	100 $\mu$ H	0.5	40 $\Omega$	1500 $\mu$ F

The gain and phase at the crossover frequency are computed as for the SC:

$$|G_{p\_ib}(j\omega_x)| = 31.737dB \quad \varphi_{p\_ib} = 89.6^\circ$$

Figure 2.6, illustrates the Bode plot of the transfer functions of the plant  $G_{p\_ib}$ .

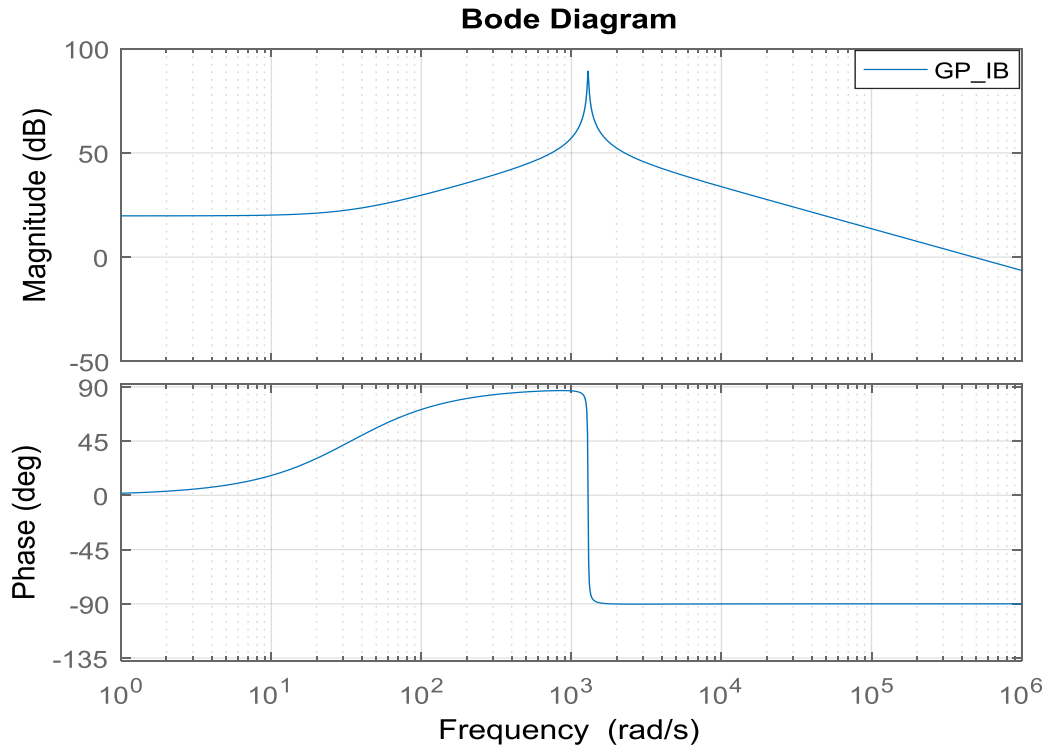
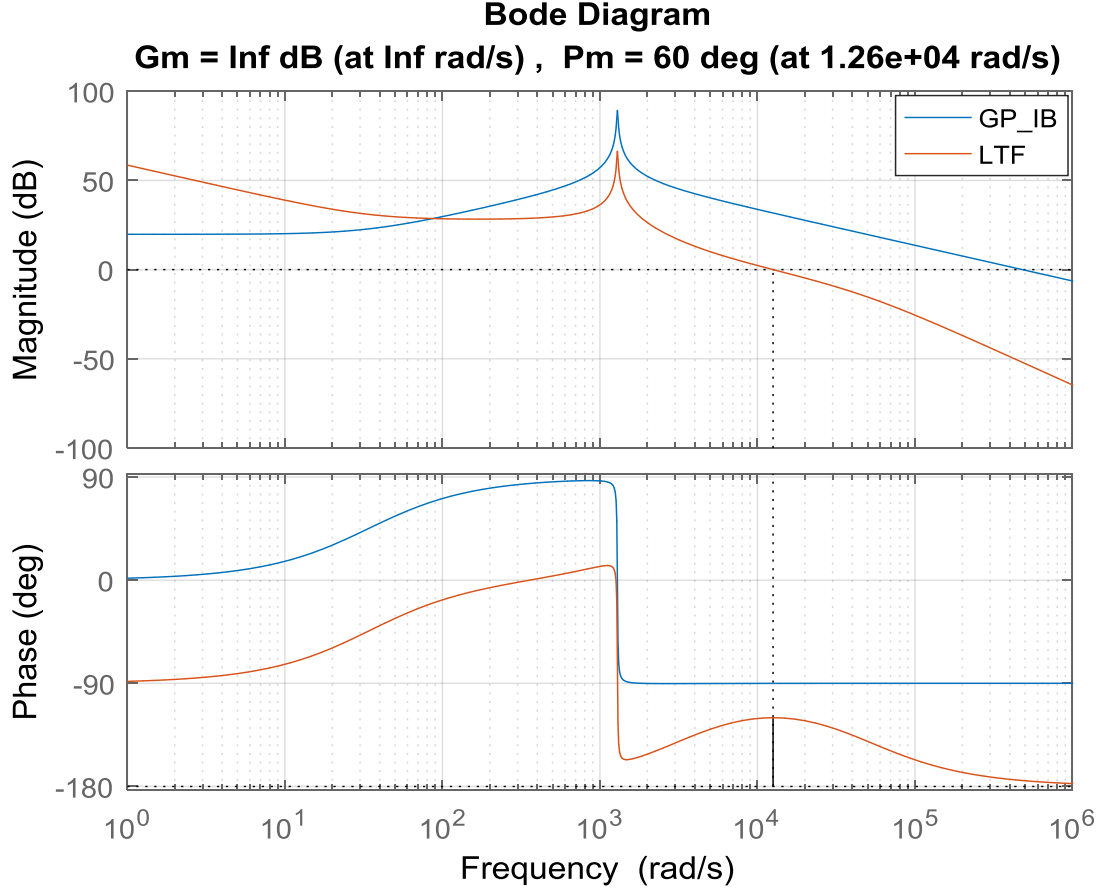


Figure 2.6: Bode plot of the plant for the design of the battery current loop

The design specifications for the battery current control loop are as follows. The crossover frequency is chosen by  $\omega_x = 2\pi f_x = 12.56$  krad/s and the phase margin  $PM = 60^\circ$  and the controller PI type II can be chosen for this plant and its parameters can be computed as for the SC.

Figure 1.7, illustrates the Bode plot of the transfer functions of the plant  $G_{p\_ib}$ , and the loop transfer function (LTF), with the designed controller. From there, one can see that the design specs ( $\omega_x = 2\pi f_x = 12.56 \cdot 10^3$  rad/sec and  $PM = 60^\circ$ ), where accomplished with the designed PI type controller.



#### 2.4.4 Design of the DC bus voltage control loop.

The voltage control loop has been designed based on, and 10 times slower than, the current control loop of the SC. The plant transfer function is given as [1]:

$$G_{p_v}(s) = \frac{v_o(s)}{i_s(s)} = \frac{R(1-D)(1 - \frac{L_s}{R(1-D)^2}s)}{2 + RCs} \quad (2-14)$$

Since, the HESS will provide the required current defined by the outer voltage loop, the bandwidth of the outer voltage control loop has to be (10 to 20 %) lesser than that of the SC current control loop. Therefore, the bandwidth is chosen as  $f_{xv} = 10\% f_{xi}$ , the BW of the SC. So, the crossover frequency becomes  $\omega_{xv} = 2\pi f_{xv} = 2.093 \text{ krad/s}$  and the phase margin PM can be selected as  $60^\circ$  using the same nominal parameters of the SC converter show in the Table 2.1.

$$G_{p_v}(s) = \frac{-1.5e^{-4}s + 26.68}{0.06s + 2} \quad (2-25)$$

At the crossover frequency one gets:

$$G_{p_v}(j\omega_x) = \frac{26.88 - j 0.314}{2 + j125.58} \quad (2-26)$$

There, the gain and phase at the crossover frequency are computed as:

$$|G_{p_v}(j\omega_x)| = -13.39 \text{ dB} \quad \varphi_{p_v} = -88.42^\circ$$

Figure 2.8, illustrates the Bode plot of the transfer functions of the plant  $G_{p_v}$ .

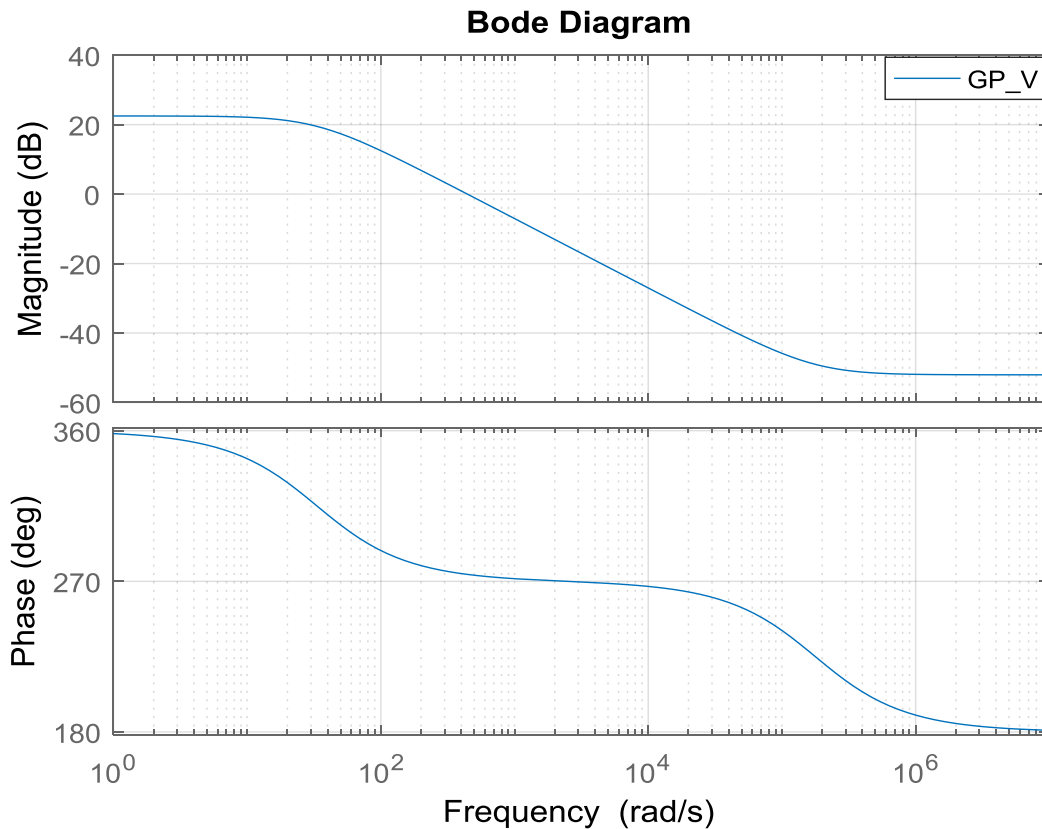


Figure 2.8: Bode plot of the plant

A simple PI type controller can be considered for this application and its parameters are computed as follows:

$$G_{pi_v}(s) = k_p + \frac{k_i}{s} \quad (2-27)$$

$$|G_{pi\_v}(j\omega_x)| = \frac{1}{|G_{p\_v}(j\omega_x)|} = 13.39dB = 4.67 \quad \text{which equal to } 10^{\left(\frac{13.39}{20}\right)} = 4.67 \quad (2-28)$$

$$|G_{pi\_v}(j\omega_x)| = \sqrt{k_p^2 + \left(\frac{k_i}{\omega_x}\right)^2} = 4.67 \quad (2-29)$$

$$\varphi_{pi\_v} = -180 + PM - \varphi_{p\_v} \quad (2-30)$$

$$\tau = \frac{\tan(\varphi_{pi\_v} + 90)}{\omega_x} \quad (2-31)$$

$$k_i = \frac{k_p}{\tau} \quad (2-32)$$

Figure 2.9, illustrates the Bode plot of the transfer functions of the plant  $G_{p\_v}$ , and the loop transfer function (LTF), with the designed controller. From there, one can see that the design specs ( $\omega_x = 2\pi f_x = 2.093 \cdot 10^3 \text{ rad/sec}$  and  $PM = 60^\circ$ ), where accomplished with the designed PI-type controller.

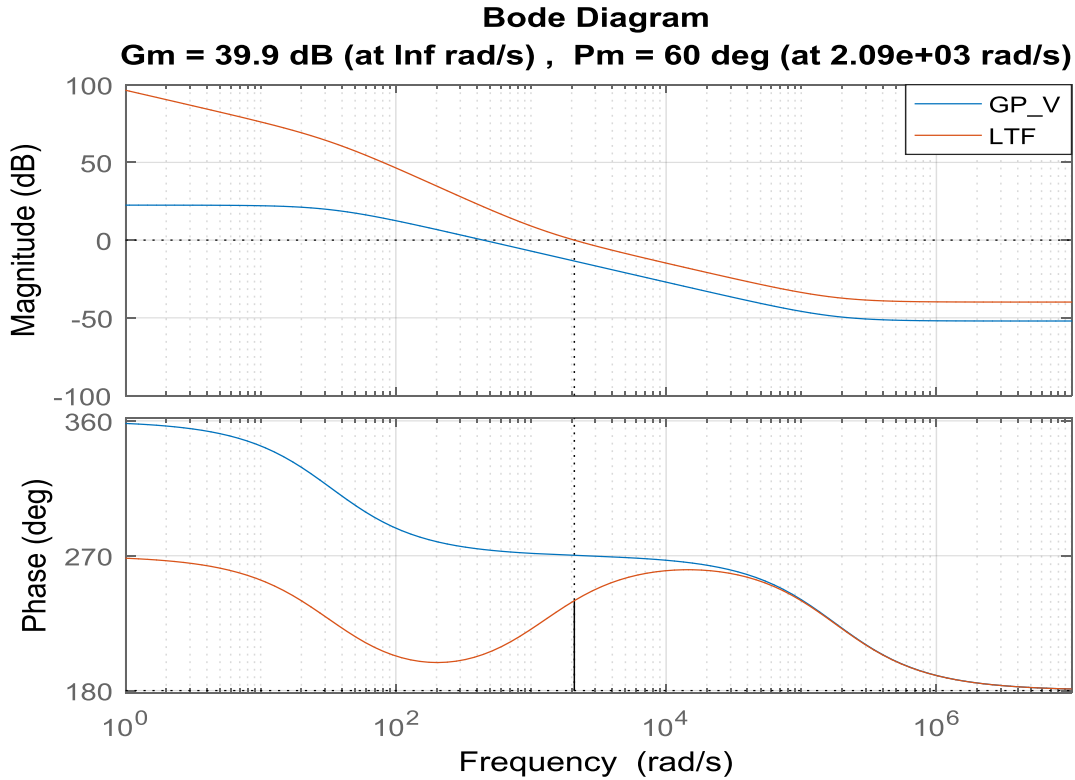


Figure 2.9: Bode plot of the voltage control loop of the HESS

## 2.5 Analysis of the operation of the PI controller for different operating conditions

The theoretical analysis for the performance of the PI controllers operating with different conditions will be presented as well as the simulation results.

Figure 2.10, illustrates the Bode plot of the transfer functions of the plant of the voltage loop  $Gp_v$ , and the LTF with a change in the voltage of the SC to  $V_{Sc} = 36$  V which will lead to a change in the duty cycle to  $D = 0.25$ . By keeping the same controllers that have been designed for  $V_{Sc} = 28.44$  V and  $D = 0.4$ , one can observe as shown in the Bode plot Fig. 2.10, that the PM and crossover frequency increase comparing with the previous/design case that was shown in Fig 2.9.

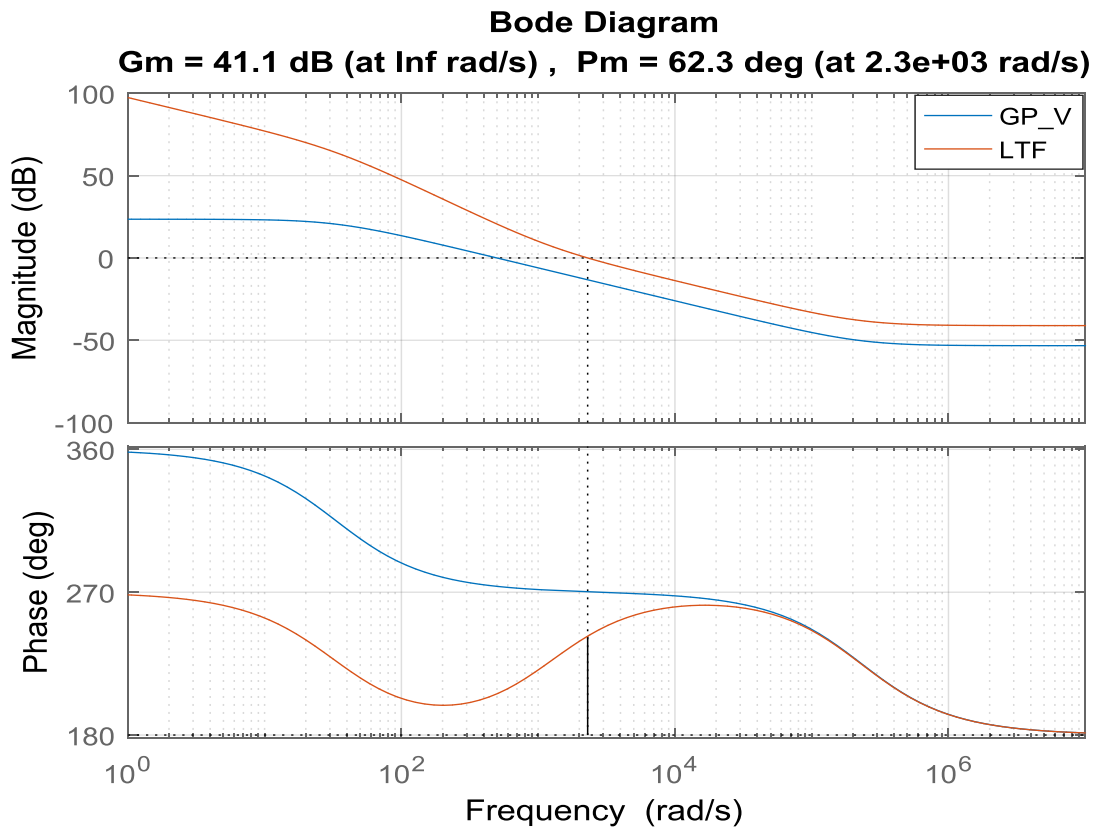


Figure 2.10: Bode plot of the plant  $Gp_v$ , and the LTF of the voltage loop.

Figure 2.11, illustrates the Bode plot of the transfer functions of the plant of the voltage loop  $Gp_v$ , and the LTF with a change in the voltage of the SC to  $V_{Sc} = 12$  V which will lead to a change in the duty cycle to  $D = 0.75$ . By keeping the same controllers that have been designed for  $D = 0.4$ , one can observe as shown in the Bode of plot Fig 2.11 that the PM and crossover frequency

decrease compared with the previous /design case that was shown in Fig 2.9. It should be noted that, in principle, the decrease in the PM should make the system more oscillatory following a disturbance and with a larger overshoot.

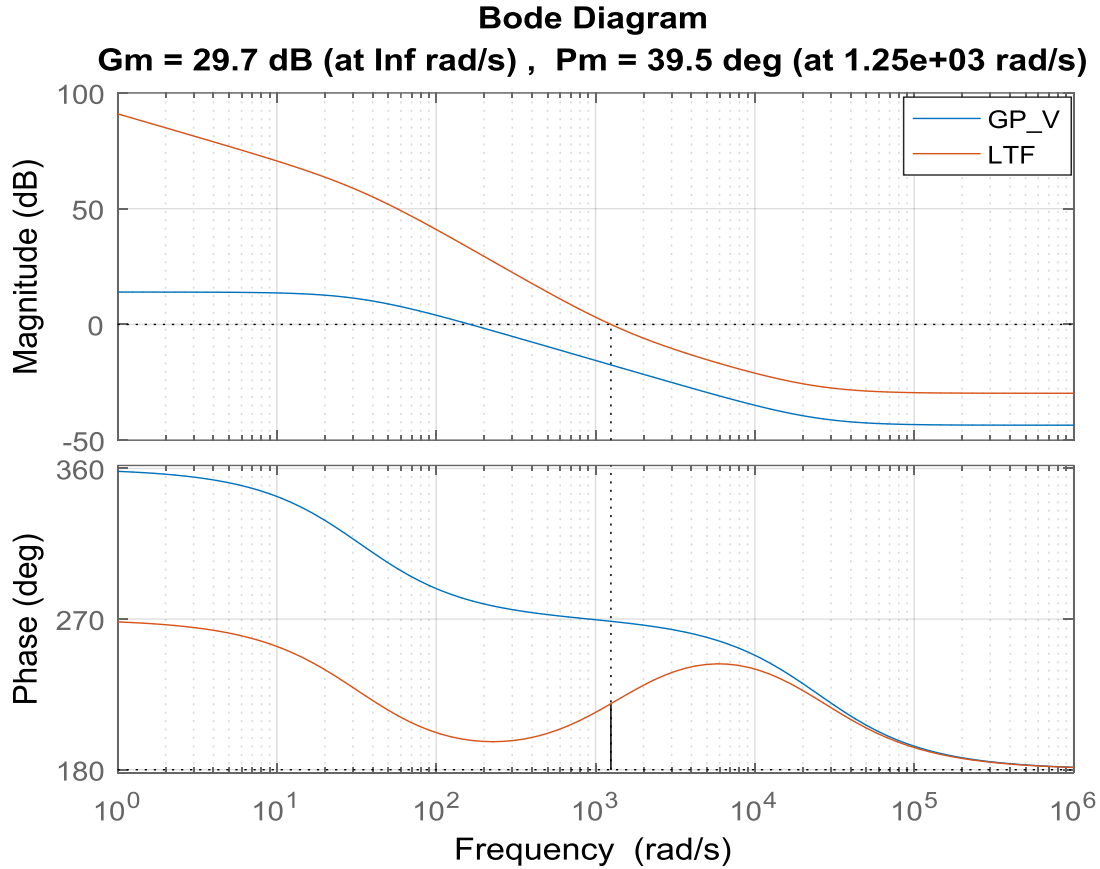


Figure 2.11: Bode plot of the plant  $Gp_v$ , and the LTF of the voltage loop.

## 2.6 Simulation results

The impact of changing the voltage across the supercapacitor and consequently the value of the duty cycle of the plant on the performance of the PI linear controller will be investigated by means of simulations. The complete system for the HESS that contains the DC bus voltage controller as well as the controllers of the inner current loops are designed for the supercapacitor working with an average voltage (28.44V) leading to  $D = 0.4$ . Then, the results obtained from it will be compared with same controller but by changing the duty cycle to  $D = 0.25, 0.75$  and this will be obtained by changing the voltage of the SC from 28.44V to 36 and 12V, respectively.

Figure 2.12, shows the results of the system with  $V_{SC} = 28.44$  V, consequently  $D = 0.4$  and a step load variation (6 to  $9\Omega$ ) is applied at  $t = 0.1$ s and at  $t = 0.3$ s the load was switched back to the original value. It can be observed, as shown by the waveforms, that the system works as expected, the DC bus voltage is regulated at 48V and battery and SC currents vary as expected.

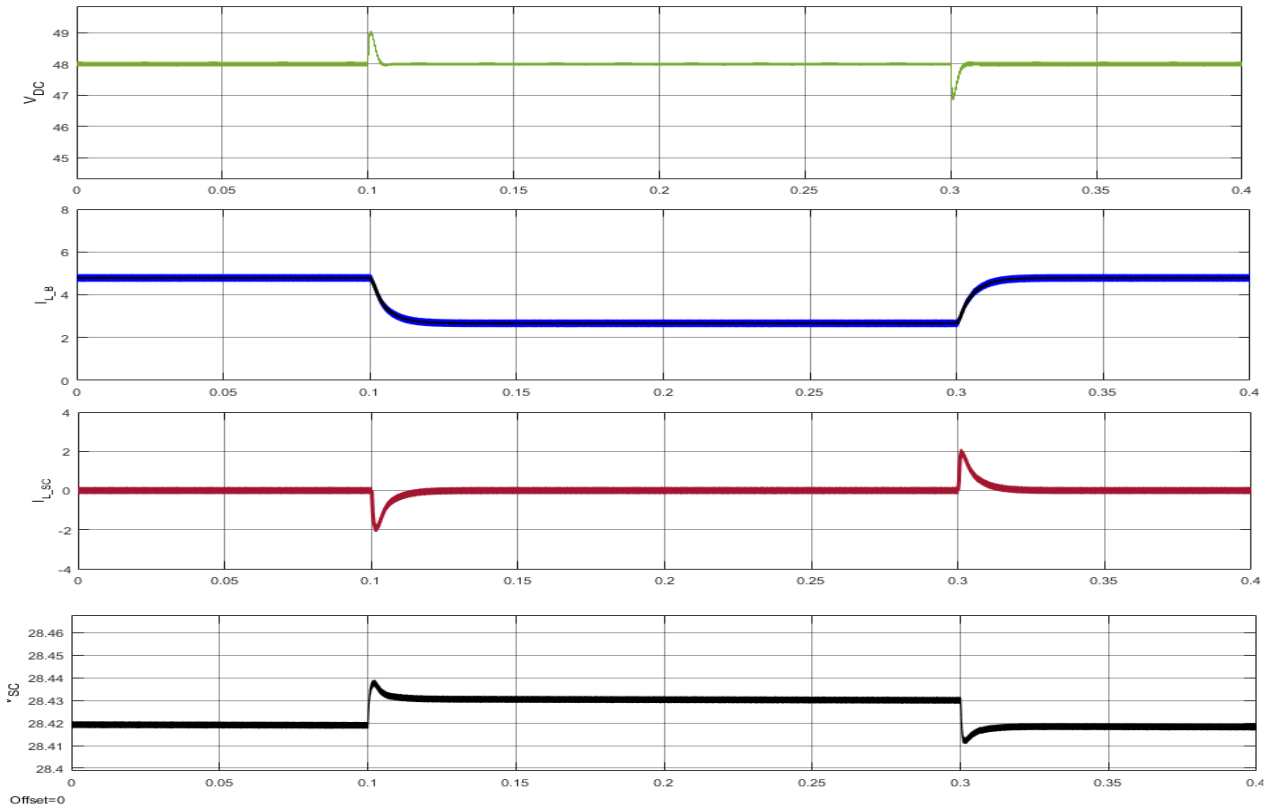


Figure 2.12: Waveforms for the system with a step load variation (6 to  $9\Omega$ ): a) DC bus voltage; b) Battery current; c) SC current; d) SC voltage

Figure 2.13, shows the results of the system with  $V_{SC} = 12$  V, consequently  $D = 0.75$  and a step load variation (6 to  $9\Omega$ ) is applied at  $t = 0.1$ s and at  $t = 0.3$ s the load was switched back to the original value. It can be observed, as shown by the waveforms, that a small oscillation appears on the DC bus voltage at the transient step as well as on the battery and SC currents. This oscillation is because of the PM, in this case smaller, as shown in the Bode plot, Fig 2.11.

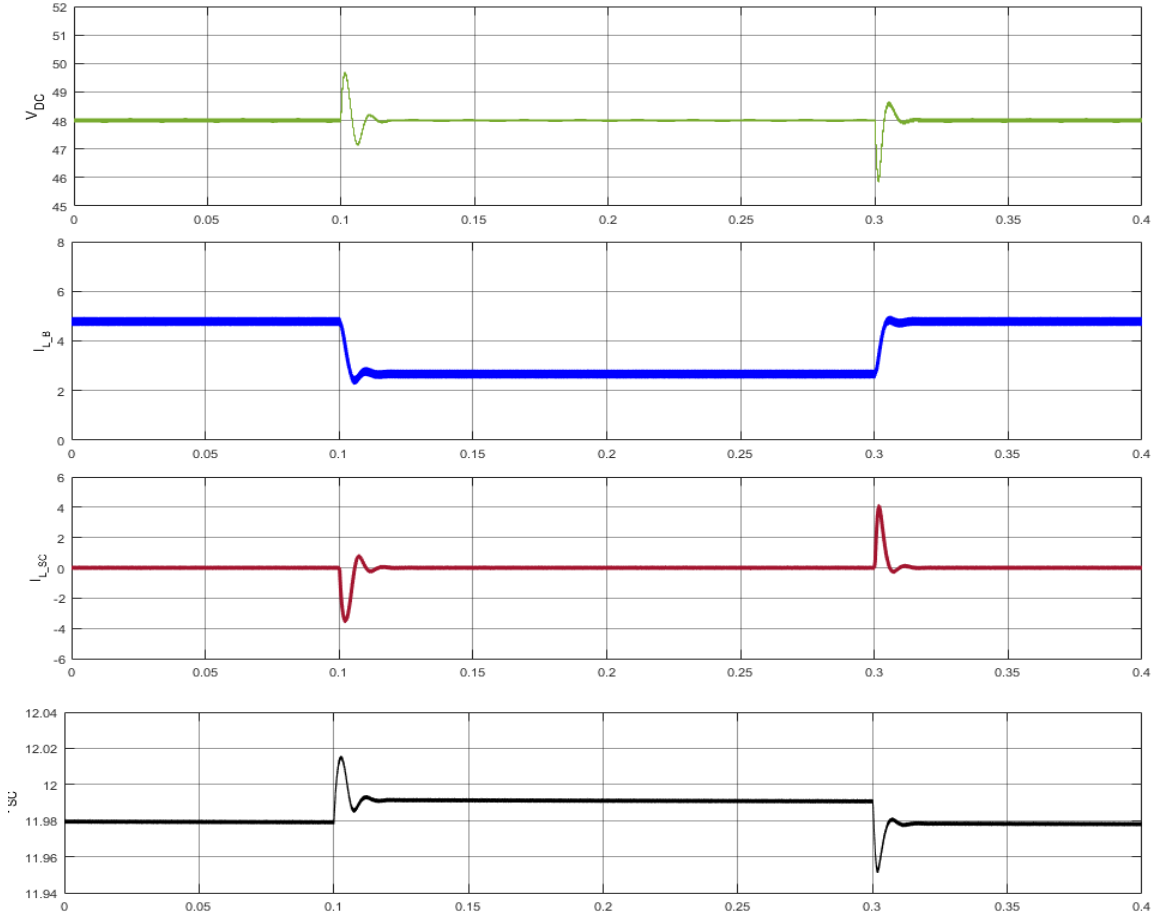


Figure 2.13: Waveforms for the system with a step load variation (6 to 9  $\Omega$ ): a) DC bus voltage; b) Battery current; c) SC current; d) SC voltage.

Figure 2.14, shows the results of the system with  $V_{SC} = 36$  V, consequently  $D = 0.25$  and a step load variation (6 to 9  $\Omega$ ) is applied at  $t = 0.1$ s and at  $t = 0.3$ s the load was switched back to the original value. It can be observed, as shown by the waveforms, that the system works as expected, the DC bus voltage is regulated at 48V with small overshoot comparing with the previous cases and battery and SC currents vary as expected.

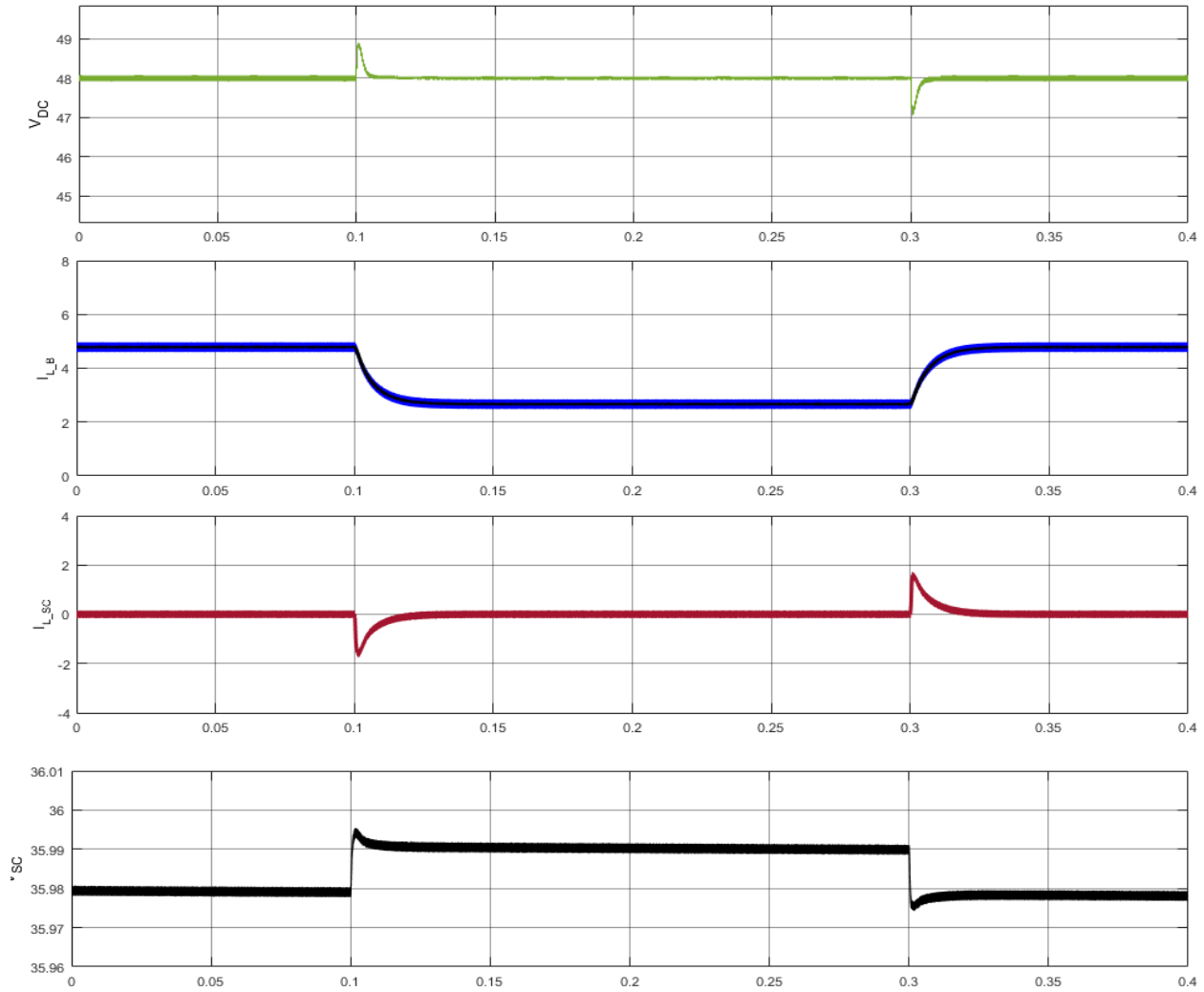


Figure 2.14: Waveforms for the system with a step load variation (6 to 9  $\Omega$ ):a)DC bus voltage; b) Battery current; c) SC current ;d)SC voltage.

Overall, the results in all cases show that the DC bus voltage is regulated at 48V in steady-state. However, the effect of changing the voltage in the supercapacitor and consequently the duty cycle and transfer function of the plant is noticeable on the transient response. As shown in the results, a small oscillation on the DC bus voltage appears at the transient step in case of  $D = 0.75$  and this oscillation occurs because the PM is only  $39.5^\circ$ . In the cases of  $D = 0.4, 0.25$  the PM =  $60^\circ, 62.3^\circ$  respectively and the system works with the expected transient response.

## 2.7 Conclusion

In this Chapter, it is shown how one can connect a hybrid energy storage system (HESS) with a PV system in to supply power to a DC load with regulated voltage. This can be done by using the class C DC-DC converter with the considered control scheme. It allows power flow to be controlled in both directions by controlling the current. The design of the controllers of the voltage and current-loops have been presented. As mentioned earlier, the main objective of the control strategy is to allow the supercapacitor (SC) to support the fast transient while the battery bank will provide the slow transient and steady-state current components, which helps to reduce the stress on the battery. This is done by using a low pass filter (LPF) with an appropriate cut-off frequency, what will be presented in the next Chapter. The impact of changing the voltage across the supercapacitor and consequently the value of the duty cycle of the plant on the performance of the PI controller was analyzed theoretical and the simulation results were presented as well.

## Chapter 3. Improving the Control Strategy of the HESS

The previous Chapter discussed the control strategy of the HESS of a DC nano-grid with a PV system as well as the design of the controllers of the voltage and current loops. In order to prevent the battery to supply fast varying and high frequency currents, one should split the required compensation current into high frequency components, to the SC, and low frequency components to the battery, what was done by means of a LPF. In this Chapter, the primary objective will be to select the cut-off frequency of the LPF so that one can control the “contribution time” of the SC which is limited by the size and energy of the SC. Besides, a new voltage control loop will be designed for a DC nano-grid connected to an AC utility grid through a single-phase ac-dc converter. It should compensate the low order harmonics in DC nano-grid created by the AC grid interface. The simulation results will be presented for all cases, stand-alone and grid connected DC nano-grid.

### 3.1 Selecting the LPF/HPF (frequency) of the HESS (SC + Batt)

As mentioned earlier, the basic control scheme of the HESS consists of a single outer voltage loop and two inner currents loops, for the inductors of the SC and battery. Either a LPF, as shown in Fig. 2.2, or a high-pass filter (HPF), considered in the following Sections, is used to split the fast (transient) and the slow (steady-state) components of the HESS reference current obtained from the outer voltage loop, and send them to the SC and battery current loops, respectively. In this Section, the choice of the cut-off frequency of the HPF, which has an impact on the duration of the contribution of the SC for the regulation of the DC bus voltage (ms, s or minute) as well as with the amount of energy the SC supplies/absorbs, is considered.

#### 3.1.1 Analysis of the HPF (frequency) on the splitting of the HESS reference current

The reference current for the HESS, required for regulating the DC bus voltage with good transient response and zero error in steady state, is provided by the DC bus voltage controller. Assuming that the battery and SC current control loops have the appropriate bandwidth, it should be realized by the SC and battery converters regardless of the way the current components are split by the HPF. Therefore, if one wishes to calculate the reference current for the SC as a response to a disturbance in the DC bus voltage, typically a variation in the current injected by the PV converter or drawn by the load, one should multiply the transfer function of the current of the HESS, as a

function of a disturbance current, by the transfer function of a HPF. This is equivalent to the full signal of the HESS current minus the battery current components, determined by the cut-off frequency of the LPF. This is shown with an elementary block diagram in Fig. 3.1.

The actual transfer function,  $I_{HESS}(s)/I_{dis}(s)$ , can be obtained by considering a disturbance current applied to the DC bus voltage, that consists of a DC bus filter capacitance ( $C_S$ ) in parallel with an equivalent load resistance ( $R$ ), fed by the HESS. The equivalent load resistance corresponds to the difference between the power consumed by the load and the power provided by the PV converter. In this analysis, it is assumed that the load demand is higher than the PV power injection, thus  $R > 0$ . Later on, by means of simulations, it will be shown that even if the HESS is absorbing power to regulate the DC bus voltage, the response of the proposed controller is still stable and well behaved.

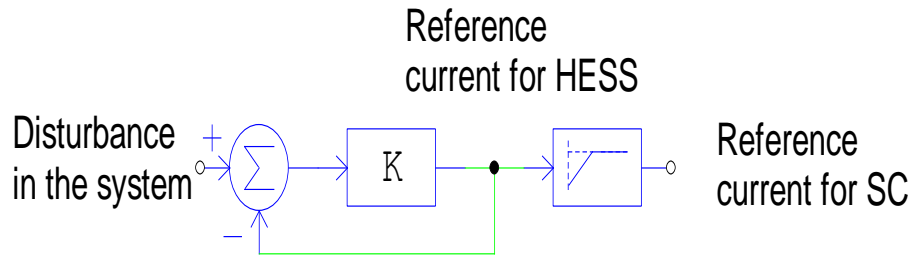


Figure 3.1: Block diagram of the system

The block diagram of the system to obtain the transfer function,  $I_{HESS}(s)/I_{dis}(s)$  is shown in Fig. 3.2. There one can see that the variation of the DC bus voltage is due to the sum of the current injected by the HESS and the disturbance current times  $R // C_S$ . Since the current control loops of the SC and battery are for their inductors, this can be reflected to the DC bus voltage side by multiplying the regulated inductor current by  $28.44/48$ , the rated voltages of the DC bus and of the storage elements, SC and battery.

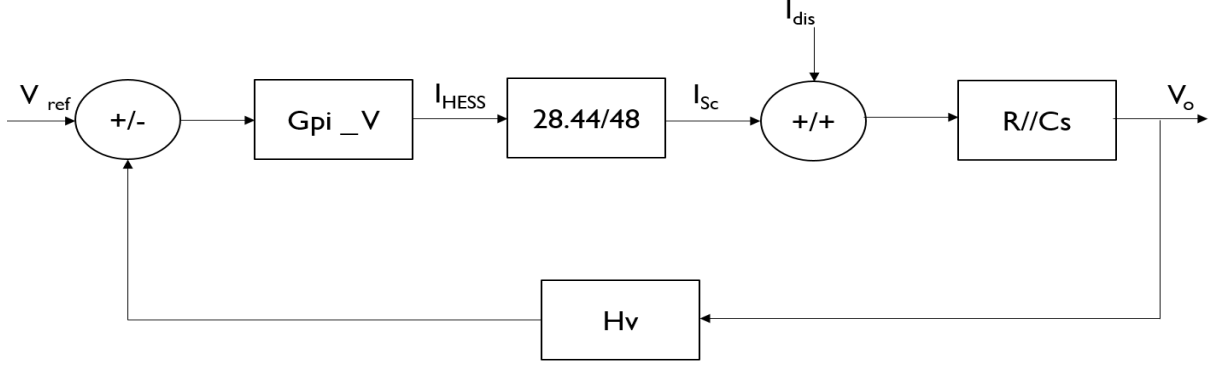


Figure 3.2: Block diagram of the equivalent system

The transfer function  $I_{HESS}(s)/I_{dis}(s)$  can then be calculated as:

$$\frac{I_{HESS}(s)}{I_{dis}(s)} = \frac{\{[R/(RC_S + 1)] Hv Gpi\_v\}}{1 + \{[R/(RC_S + 1)] Hv Gpi\_v (28.44/48)\}} \quad (3-1)$$

Where

$$G_{pi\_v}(s) = K_P + \frac{K_i}{s}$$

Next, one can compute the response of the reference current of the SC as a function of the disturbance current and the HPF transfer function. Thus,

$$\frac{I_{SC}(s)}{I_{dis}(s)} = \frac{I_{HESS}(s)}{I_{dis}(s)} HPF(s) \quad (3-2)$$

$$\frac{I_{SC}(s)}{I_{dis}(s)} = \frac{\{[R/(RC_S + 1)] Hv Gpi\_v\}}{1 + \{[R/(RC_S + 1)] Hv Gpi\_v (28.44/48)\}} HPF(s) \quad (3-3)$$

Where

$$HPF(s) = \frac{s \tau}{1 + s \tau} \quad (3-4)$$

To determine the cut-off frequency of the HPF to force the SC to provide a certain “contribution” to the regulation of the DC bus voltage, one can choose and impose how long the

SC will inject current. Based on this, the value of  $\tau$  can be defined. The equation below represents the response of a 1<sup>st</sup> order HPF.

$$C(t) = Ae^{-\frac{t}{\tau}} u(t) \quad (3-5)$$

Where:

$u(t)$  is a step input.

To simplify the analysis, let's assume that the rise time corresponds to the time ( $T$ ) when the output reaches 10% of its steady-state value.

Then

$$C(t) = 0.1 u(t) \quad (3-6)$$

From (3-5) and (3-6)

$$0.1 u(t) = e^{-\frac{t}{\tau}} u(t)$$

$$0.1 = e^{-\frac{t}{\tau}}$$

$$t = 2.3 \tau$$

From this equation, we can select for how long ( $T$ ) the SC will injected current.

$$f = \frac{2.3}{2 \pi T} \quad (3-7)$$

This equation will be evaluated with three different times ( $T$ ) as shown in the Table below to see the impact on the action of the supercapacitor reference current.

Table 3.1: Time of contribution of the SC and cut-off frequency of the HPF

Time (s)	Cut-off frequency (Hz)
1	0.37
10	0.037
100	0.0037

Fig. 3.3, shows the response of the current of the SC to a step variation in the distortion current with the cut-off frequency ( $f$ ) at 0.37, 0.037, 0.0037 Hz and without a HPF, what corresponds to the total current that should be drawn from the HESS ( $I_{HESS}$ ). There one can see that as the cut-off frequency decreases, the duration of the pulse of current of the SC increases as expected. Due to the 28.44 /48 gain in the transfer function, in steady state and for the case of “no-HPF”, the current injected by the HESS should be equal to about 1.5 as can be seen in Fig. 3.3. Also, that for the curve with  $f = 0.0037$  Hz cut-off frequency, one can see that the current contribution of the SC reaches 10% of the final value, i.e. 0.15 A, at  $t \sim 100$  s.

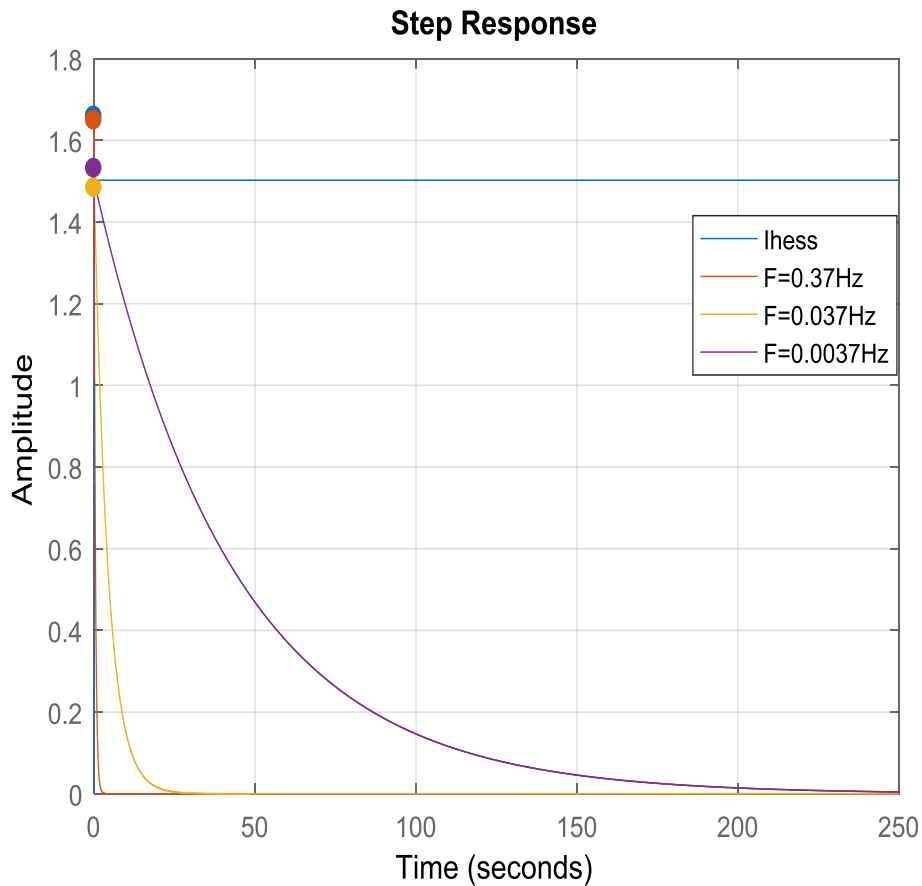


Figure 3.3: Step responses of the  $\frac{I_{sc}}{I_{dis}}(s)$  and  $\frac{I_{HESS}}{I_{dis}}(s)$  with different values of the cut-off frequency of the HPF

Fig. 3.4, shows the curve with  $f = 0.37$  Hz, with a narrow time range, 1s. One can see that the current contribution of the SC drops to 10% of the final value 1.5A, i.e. 0.15 A, at  $t \sim 1$  s, as expected based on Table 2.3.

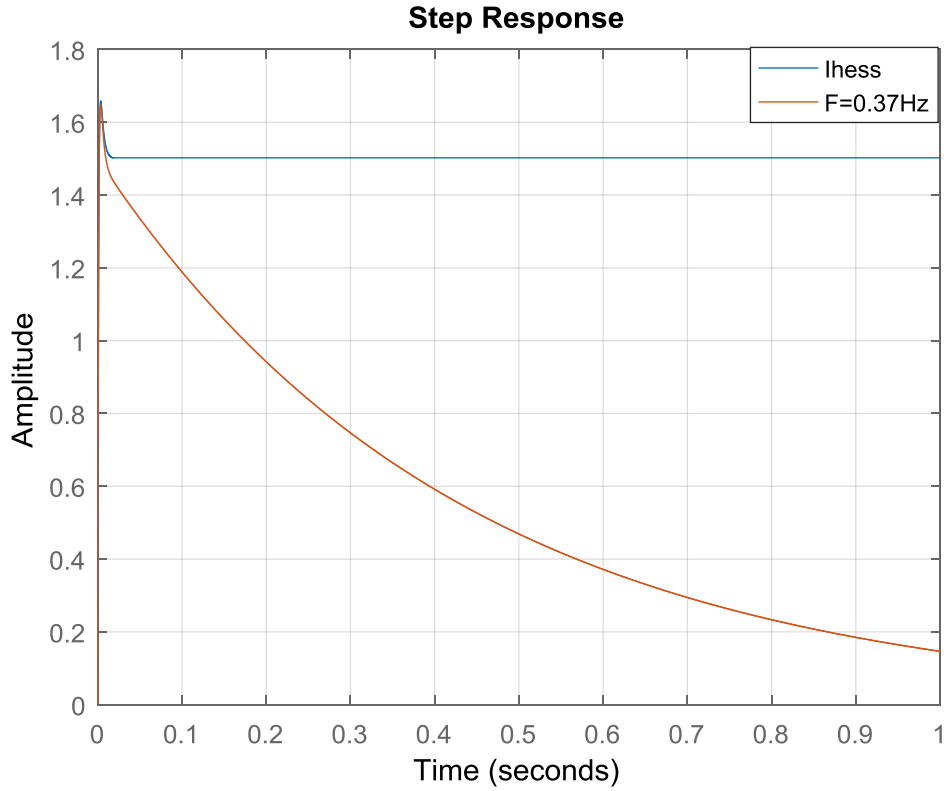


Figure 3.4: Step responses of the  $\frac{I_{sc}}{I_{dis}}(s)$  and  $\frac{I_{HESS}}{I_{dis}}(s)$  with cut-off frequency of HPF  $f = 0.37$  Hz.

### 3.1.2 Simulation results

The validation of the approach for calculating the cut-off frequency of the HPF that yields the desired “time of contribution” of the SC for the regulation of the DC bus voltage following a step-like current distortion is carried out by means of simulation. This was done using PSIM and the power circuit discussed in Fig. 2.1 and control scheme shown in Fig. 2.2. The controllers of the inner current loops and the outer voltage loop are those designed in previous Sections. The main objective of this Section is to observe the reaction of the DC bus voltage as well as the currents of the SC and battery as one changes the cut-off frequency of the HPF, what should lead to the times ( $T$ ) stated in Table 3.1. Besides, one will compute the energy supplied/absorbed by the SC, which can be defined by

$$E = \int P dt, \quad E_{SC} = \int V_{SC} I_{SC} dt. \quad (3-8)$$

Fig. 3.5, shows the results of the system with a LPF with a cut-off frequency  $f = 0.37\text{Hz}$  for a step load variation ( $9$  to  $6 \Omega$ ) applied at  $t = 3\text{s}$ . It can be observed, as shown in the waveforms, that SC presents  $T = 1\text{s}$  contribution, then it returns to zero as expected, with a supply of energy of  $43\text{Wh}$ .

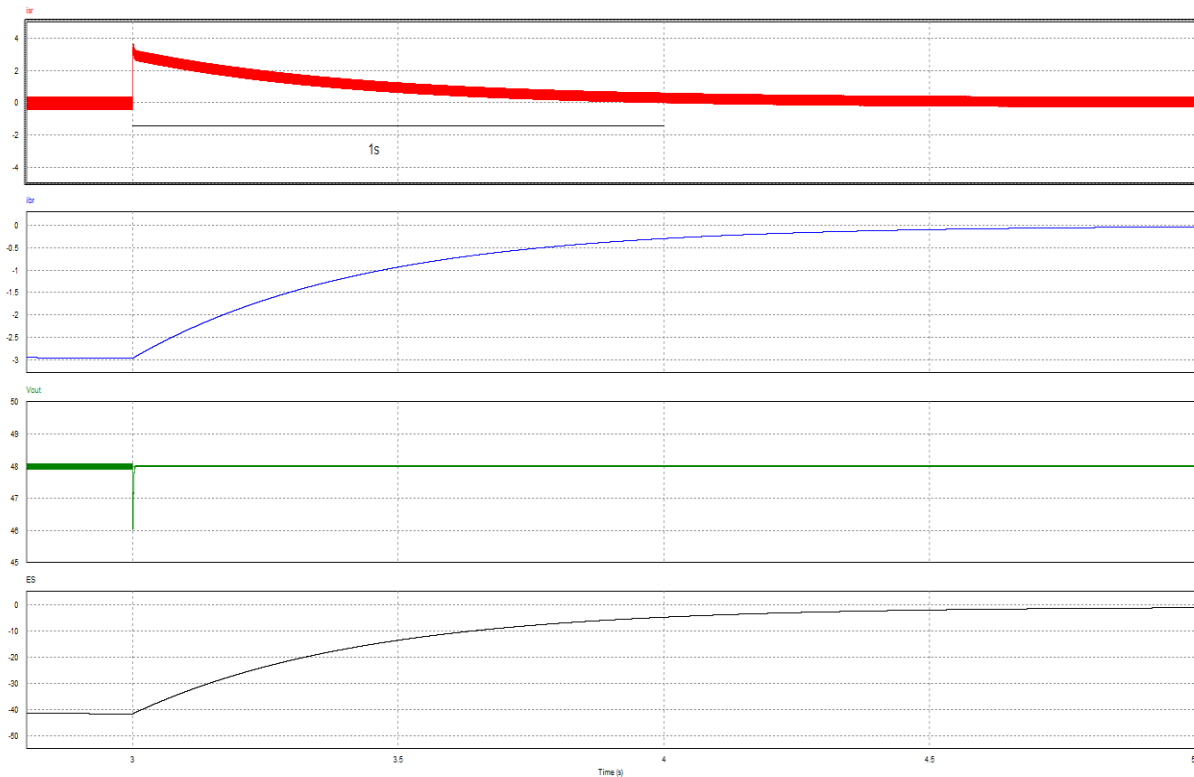


Figure 3.5: Waveforms for the system with  $f = 0.37\text{Hz}$  for a step load variation ( $9$  to  $6 \Omega$ ) applied at  $t = 3\text{s}$ : a) SC current; b) Battery current; c) DC bus voltage; d) Energy supplied by the SC.

In the second test, as shown in Fig. 3.6, the cut-off frequency of the LPF is selected to be  $f = 0.037\text{Hz}$ . The same step load variation ( $9$  to  $6 \Omega$ ) is applied at  $t = 12\text{s}$ . It can be observed in the waveforms that the SC presents a  $T = 10\text{s}$  contribution, then it returns to zero as expected, with a supply of energy of  $430\text{Wh}$ .

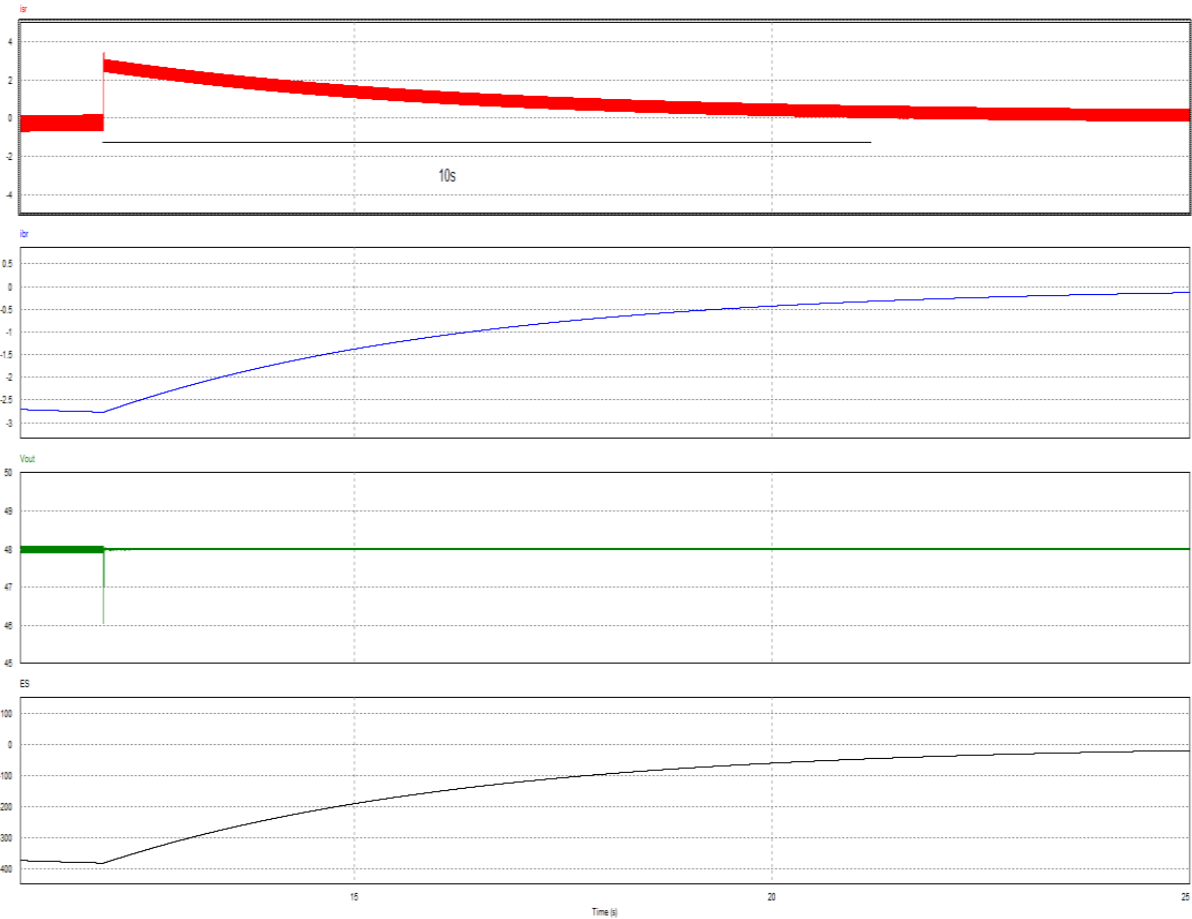


Figure 3.6: Waveforms for the system with  $f = 0.037\text{Hz}$  for a step load variation ( $9$  to  $6 \Omega$ ) applied at  $t = 3\text{s}$ : a) SC current; b) Battery current; c) DC bus voltage; d) Energy supplied by the SC..

In the last test, the cut-off frequency of the LPF is selected to be  $f = 0.0037\text{Hz}$  for a step load variation ( $9$  to  $6 \Omega$ ) applied at  $t = 120\text{s}$ . As shown in Fig. 3.7, it can be observed that the SC presents a  $T = 100\text{s}$  contribution, then it returns to zero as expected with a supply of energy of  $4300\text{Wh}$ .

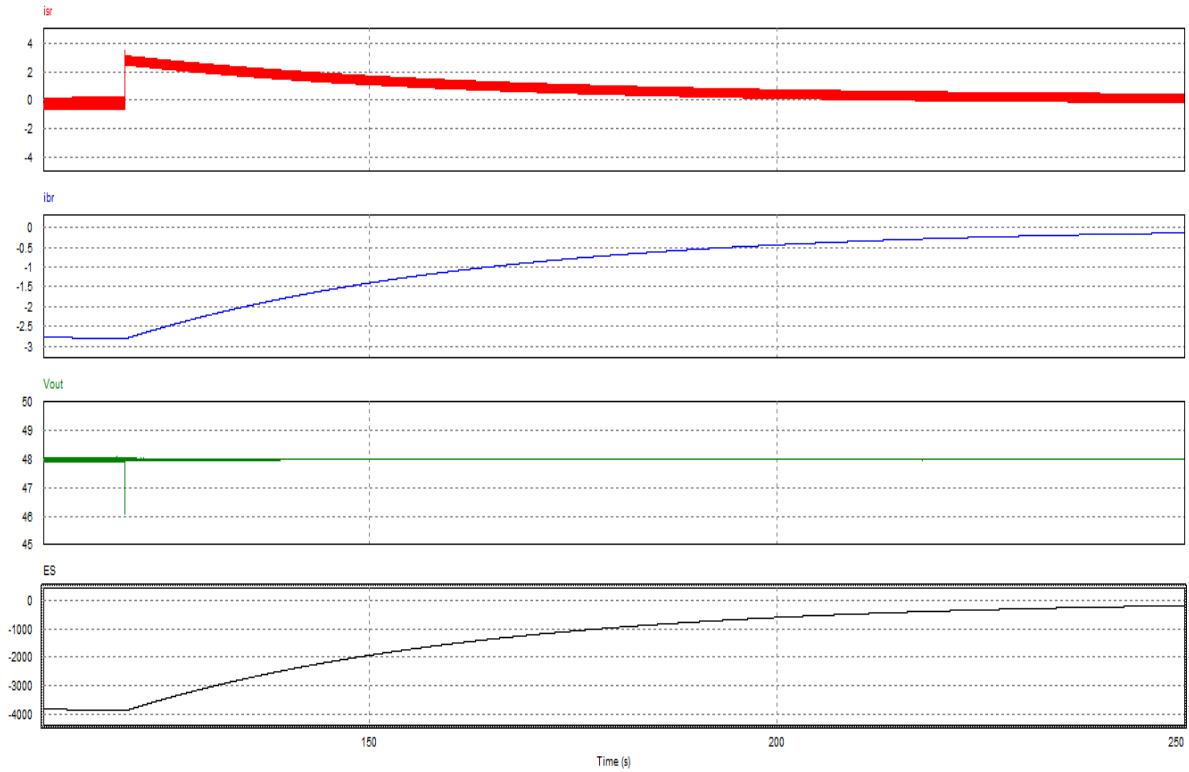


Figure 3.7: Waveforms for the system with  $f = 0.0037\text{Hz}$  for a step load variation ( $9$  to  $6\ \Omega$ ) applied at  $t = 3\text{s}$ : a) SC current; b) Battery current; c) DC bus voltage; d) Energy supplied by the SC.

### 3.2 A voltage control loop for the SC

The SC should have a voltage regulation loop to prevent its voltage level to be too high, what could damage it, or too low, when the available energy for regulating the DC bus voltage could be insufficient. For the choice of the reference value, one can select one that allows the SC to supply a given amount of energy before reaching 50% of its rated voltage, and absorb this same amount of energy, before reaching 100% of its rated voltage. By setting the reference voltage at 79% of the rated value, the SC has a state-of-charge with equal energy capacity to supply and absorb power before reaching the limit voltage values. This voltage loop should not interfere much with the SC's main task of supplying and absorbing fast varying currents to regulate the DC bus and prevent the battery from a high current stress. Therefore, this control loop should be slow, attempting to charge/discharge the SC with low values of currents, which could come from either the PV panel or from the battery.

### 3.2.1 Design of the voltage control loop for the SC.

Fig. 3.8, shows the block diagram of the SC voltage control loop. It includes the inner inductor current ( $I_{l\_sc}$ ) control loop with a PI-type II controller ( $Pi\_isc$ ) and the duty-cycle to inductor current transfer function ( $Gi\_sc$ ), which was discussed in a previous Section. Since the current control loop is expected to be much faster than SC voltage control loop, it can be represented as a simple gain ( $1/H\_isc$ ). For the regulation of the SC voltage, it is measured and compared to a reference voltage. The error is passed through a low bandwidth PI-type controller ( $Pi\_vsc$ ) to produce the slow varying current required to bring the SC voltage towards the reference value. This current is added to the fast one ( $Iref\_sc$ ), discussed in a previous Section, to provide the fast varying current component of the HESS. For the design of the outer SC voltage loop, one needs to know how the inductor current of the SC affects the voltage in the SC. This relation, transfer function ( $Gv\_sc$ ), can be obtained from the power converter and SC shown in Fig. 2.3.

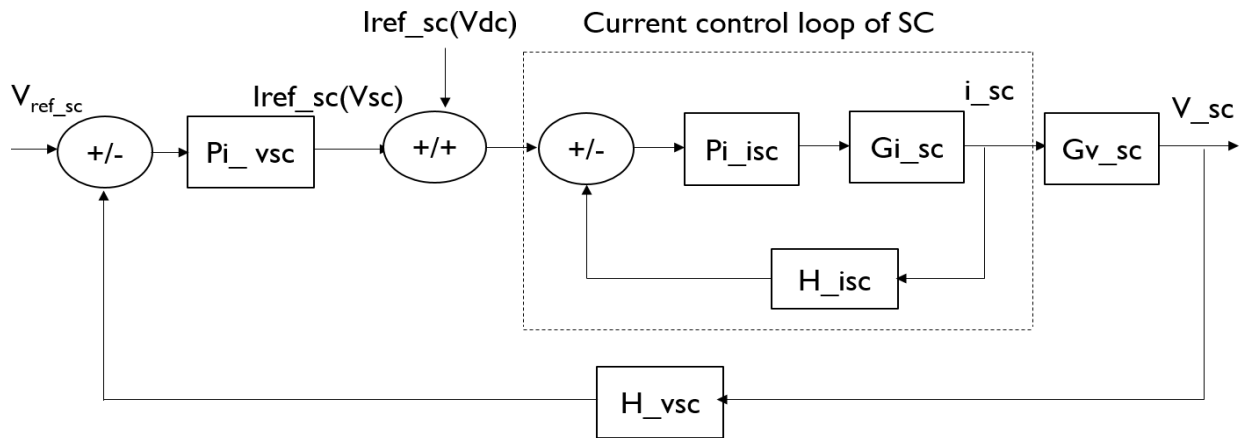


Figure 3.8: Block diagram of the SC voltage control loop.

The “plant” for the design of the closed loop controller for the voltage of the SC ( $Gv\_sc$ ) is based on a relation between the SC current and the SC voltage.

Calculating the plant transfer function ( $Gv\_sc$ ):

- State equation

$$C \frac{dV_{sc}}{dt} = i_{l\_sc} \quad (3-9)$$

- Using Laplace transform

$$Cs v_{sc}(s) = i_{l_{sc}}(s) \quad (3-10)$$

- The plant is then:

$$Gv_{sc}(s) = \frac{V_{sc}(s)}{i_{l_{sc}}(s)} = \frac{1}{Cs} \quad (3-11)$$

The voltage control loop for the supercapacitor should be slower than the inner current loop as well as than the voltage control loop for the DC bus. Therefore, the bandwidth of the voltage control loop for supercapacitor is chosen as  $10\% f_{xv}$ , where  $f_{xv}$  is the BW of the outer DC bus voltage loop, and the phase margin  $PM = 60^\circ$ . In such a case, a PI type II controller can be selected.

The transfer function of the PI type II controller is:

$$Pi_{vsc}(s) = \frac{Ki(1 + s\tau)}{s\tau(1 + sTp)} \quad (3-12)$$

The parameters of the main element of the plant (SC) and designed controller, computed using the approach described in previous Sections, are shown in Table 3.2.

Table 4.1: Parameter of the PI controller for the SC voltage control loop.

C	Ki	$\tau$	Tp
1F	38.1	0.098s	7ms

The scheme of the control system for the HESS shown in Fig. 2.2, was modified as shown in Fig. 3.9. Now, the complete control scheme includes a voltage control loop to keep the voltage of the SC loosely regulated, due to the low BW, around a reference value.

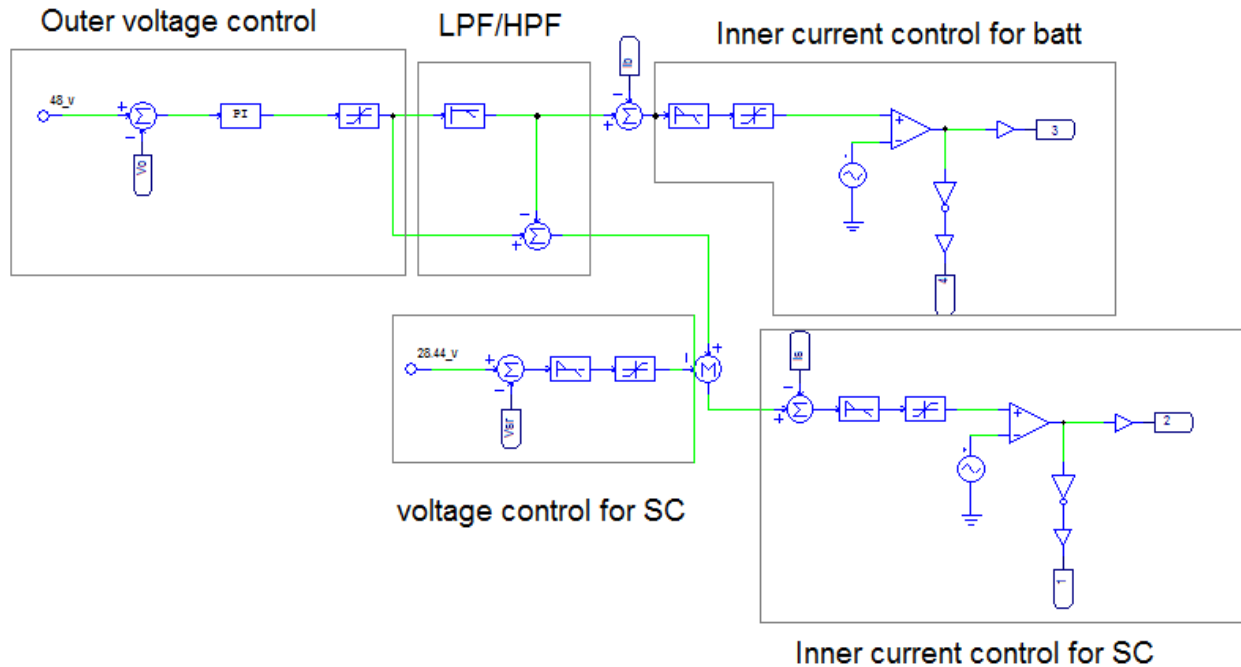


Figure 3.9: Control scheme of the HESS.

### 3.2.2 Simulation results

Considering the HESS control scheme shown in Fig. 3.9, the simulation results were obtained with parameters that have been presented previously for the voltage control loops and current control loops as well as the converter parameters. The objective is to investigate the potential benefits of including the voltage loop to the SC control loop. To observe the benefit of the SC voltage control loop, the system will be tested with and without the SC voltage control loop.

Fig. 3.10, shows the results of the system without the voltage control loop of the SC. A step load variation (40 to 20  $\Omega$ ) is applied at  $t = 0.1s$ . It can be observed, as shown in the waveforms, that the voltage of the SC increases and it does not return to the original voltage. But at  $t = 0.3$  it is back at the original value, when the load was switched back to the system. The issue is that the voltage of the SC will vary according to the load variations, which can make it increase or decrease continuously. With the SC voltage control loop, the voltage age the SC tends to return to the reference value.

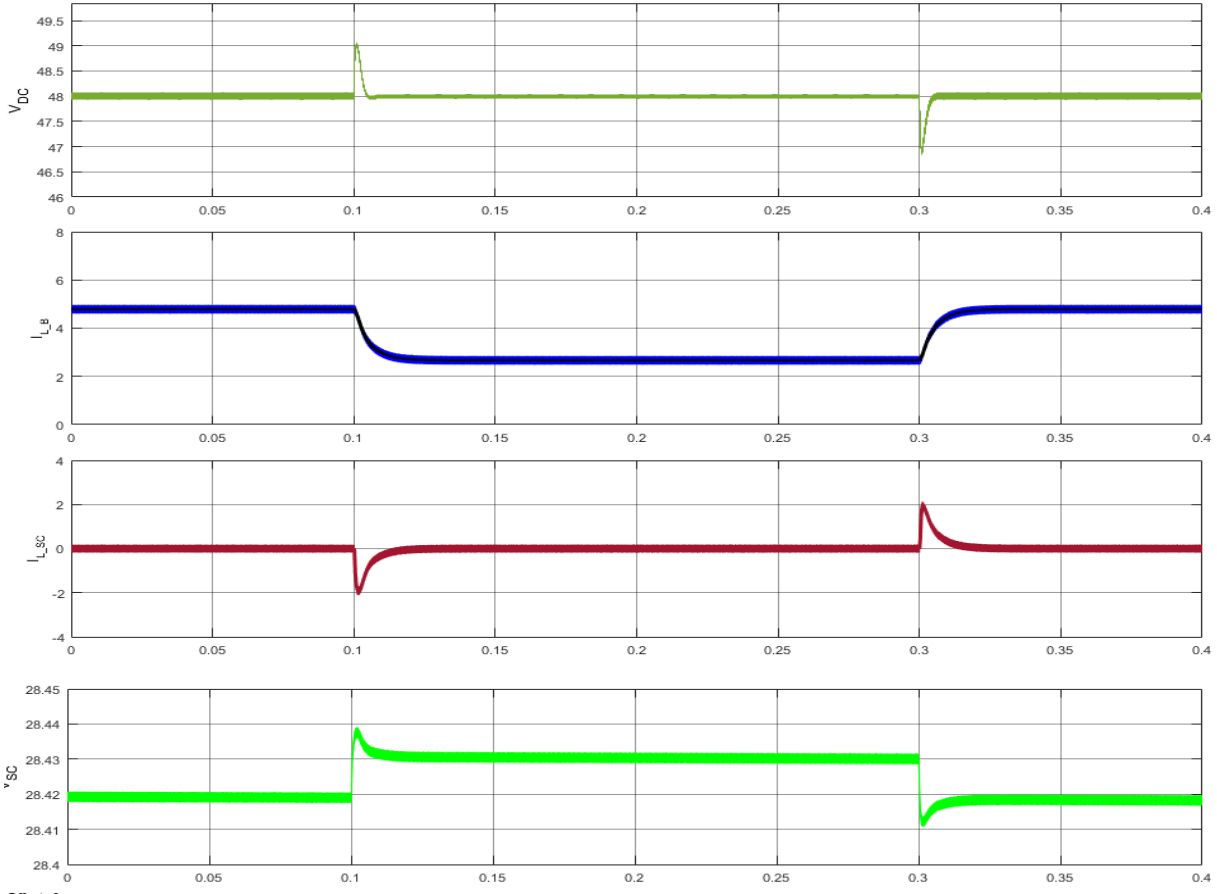


Figure 3.10: Waveforms for the system without voltage control for SC: a) DC bus voltage; b) Battery current; c) SC current; d) SC voltage.

Fig. 3.11, shows the results of the system with the SC voltage control loop. A step load variation (40 to 20  $\Omega$ ) is applied at  $t = 0.1s$ . It can be observed, as shown in the waveforms, that the voltage of the SC changes with the step variations in the load and then the voltage control loop of SC forces the voltage of SC to return to its desired value. Moreover, the voltage control loop of the SC did not affect significantly the SC current required to regulate the DC bus voltage since it is slower than the DC bus voltage control loop.

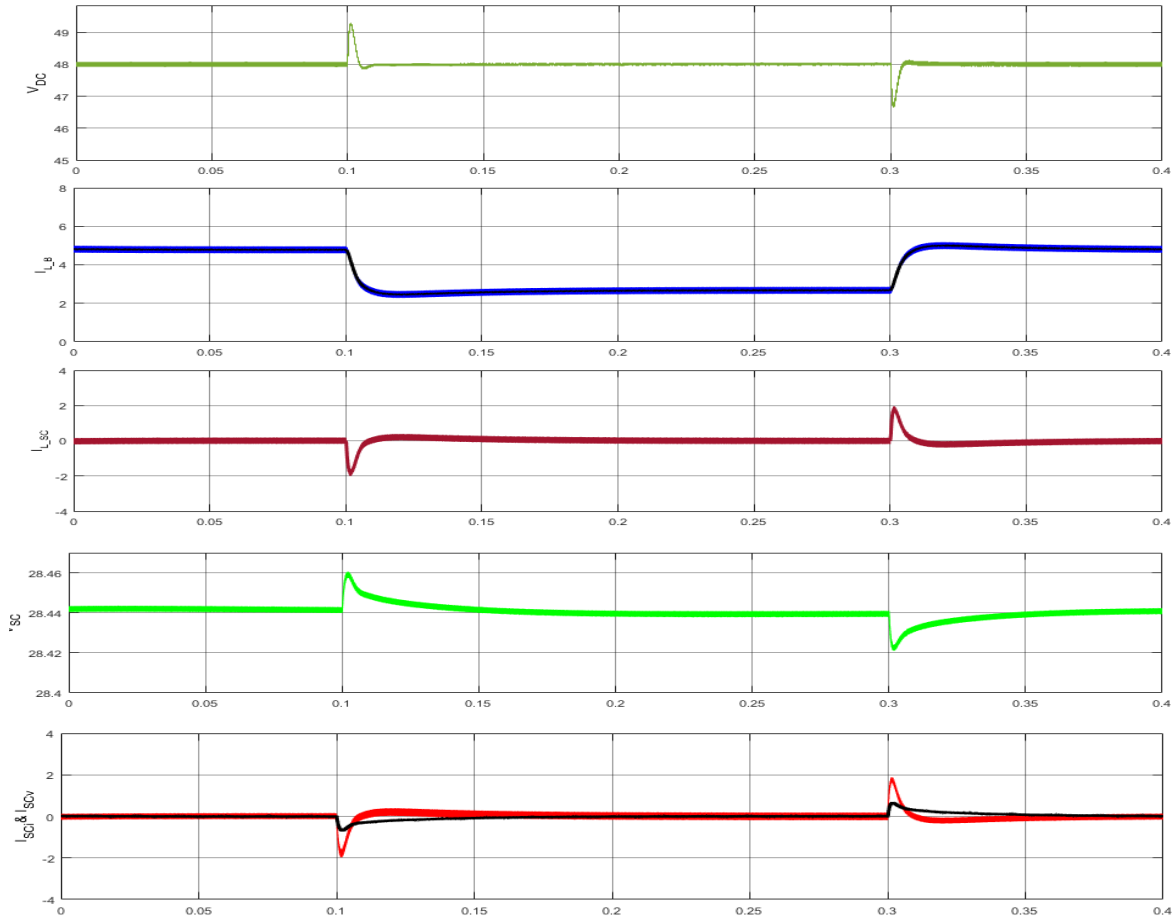


Figure 3.11: Waveforms for the system without voltage control for SC: a) DC bus voltage; b) Battery current; c) The actual SC current; d) SC voltage; e) The two reference currents of the SC.

### 3.3 A voltage control loop to compensate the low order harmonics of the grid interface.

The photovoltaic (PV) systems deployed at residential locations have been concerned more with electricity generation for AC loads and grids, as shown in Fig. 3.12. Since the renewable energy source generates DC power, the generated power must be converted to AC, what is performed by a DC-AC converter or inverter. Once the inverter is connected to the DC system and it is bidirectional power flow, it draws a DC component as well as an AC current component, leading to a voltage ripple of twice the AC side fundamental frequency. Typically, this occurs for single-phase interfaces to an AC grid and it is known that single-phase inverters require a large electrolytic capacitor to filter the voltage ripple at the DC bus. It should be noted that this device

has a short life span, and ideally should be replaced with a small film type capacitor, what would require an “active” means for attenuating the second order voltage ripple [7].

The residential DC nano-grid discussed thus far has been of the stand-alone type. Ideally, for the sake of making sure that the DC loads can be fed even in the absence of renewable power generation and availability of energy in the storage units, an AC grid connection is desirable. In such a system, it is envisaged that instead of using an inverter with a large electrolytic capacitor, to mitigate the 2<sup>nd</sup> order voltage ripple at the DC bus, one can make use of the HESS to provide the 2<sup>nd</sup> order current component required to counteract the one produced by the AC grid connected inverter [5], [6]. The following Sections discuss an approach to achieve this goal.

As depicted in Fig. 3.12, PV systems with HESS are usually build with a Proportional-Integral (PI) controller in the voltage control loop [8]. In order to achieve zero steady-state error and reject disturbance on the DC bus voltage with the HESS, a Proportional-Integral (PI) controller with a resonant (R) component will replace the conventional PI controller. The designing of the PI+R voltage loop controller will be discussed next.

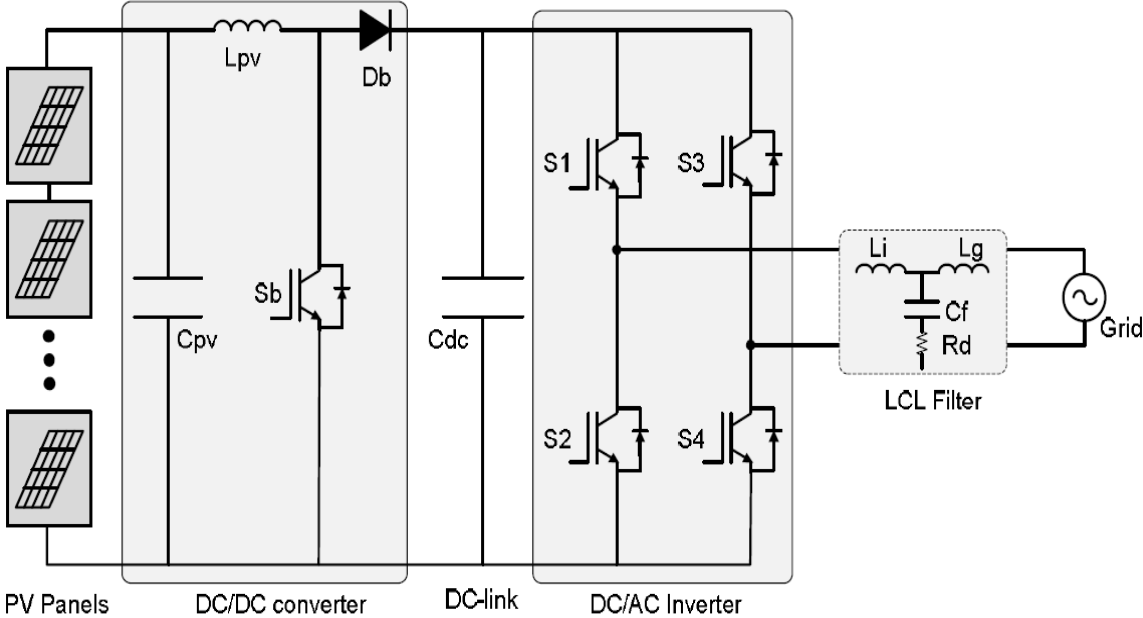


Figure 3.12: PV system with a single-phase dc/ac converter [8].

### 3.3.1 Design of a voltage control loop to compensate the low order harmonics in the DC nano-grid.

The task of regulating the voltage at the DC bus/nano-grid discussed thus far relied on the HESS. It employed PI type controllers to make sure that the DC voltage is regulated at the rated value (48 V) in steady state with a fast and damped dynamic response. The zero error in steady-state due to step load variations is achieved by the integrator component of the PI controller which presents an infinite gain at DC (0 Hz). However, its gain at 120 Hz, the frequency of the ripple created by the inverter, is not high enough to keep the magnitude of this ripple at a low value. In order to reject this disturbance, a proportional integral plus resonant (PI+R) controller will replace the original PI controller. The PI+R controller is able to introduce a high gain at the frequency of the disturbance, its resonant frequency, so it can significantly attenuate the voltage ripple at 120Hz.

The transfer function of the PI+R controller is given by

$$G_{pi\_v}(s) = k_P + \frac{k_i}{s} + \frac{2K_i' \omega_c s}{s^2 + 2\omega_c s + \omega_0^2} \quad (3-13)$$

Where  $K_p$  and  $K_i$  are the gain constants of the original PI controller. The resonant term is tuned at the frequency of the disturbance,  $\omega_0 = 2\pi 120$  rad/s.

There are two parameters to be selected:  $k_i'$  and  $\omega_c$ . These are the DC gain of the resonant term and the bandwidth, typically of  $10\pi$  rad/s, around the resonance frequency. In principle, by increasing  $K_i'$  one should get a higher gain at  $\omega_0$ , what should attenuate more the disturbance signal, but would not affect the phase angle of the controller. This can be observed in Fig. 3.13, for  $\omega_0 = 2\pi 120$ ,  $\omega_c = 10\pi$  rad/s and  $K_i' = 1$  and 10.

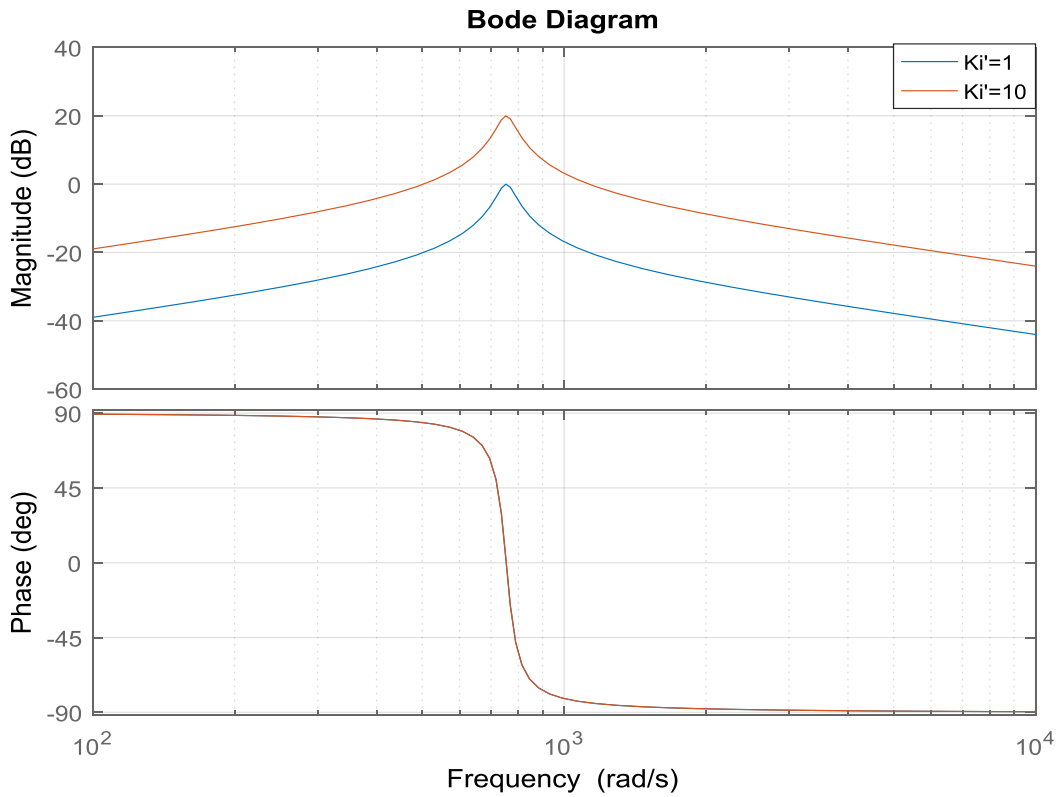


Figure 3.13: Frequency responses of a non-ideal PI+R controller when  $K_i'$  changes.

The second parameter to be selected is  $\omega_c$ . In principle, by increasing  $\omega_c$  one should get a wider range of frequencies benefiting from the gain at the resonant frequency, but it would not affect the gain at  $\omega_0$ . This can be observed in Fig 3.14, for  $\omega_0 = 2\pi 120$ ,  $K_i' = 10$  and  $\omega_c = \pi$  and  $10\pi$  rad/s.)

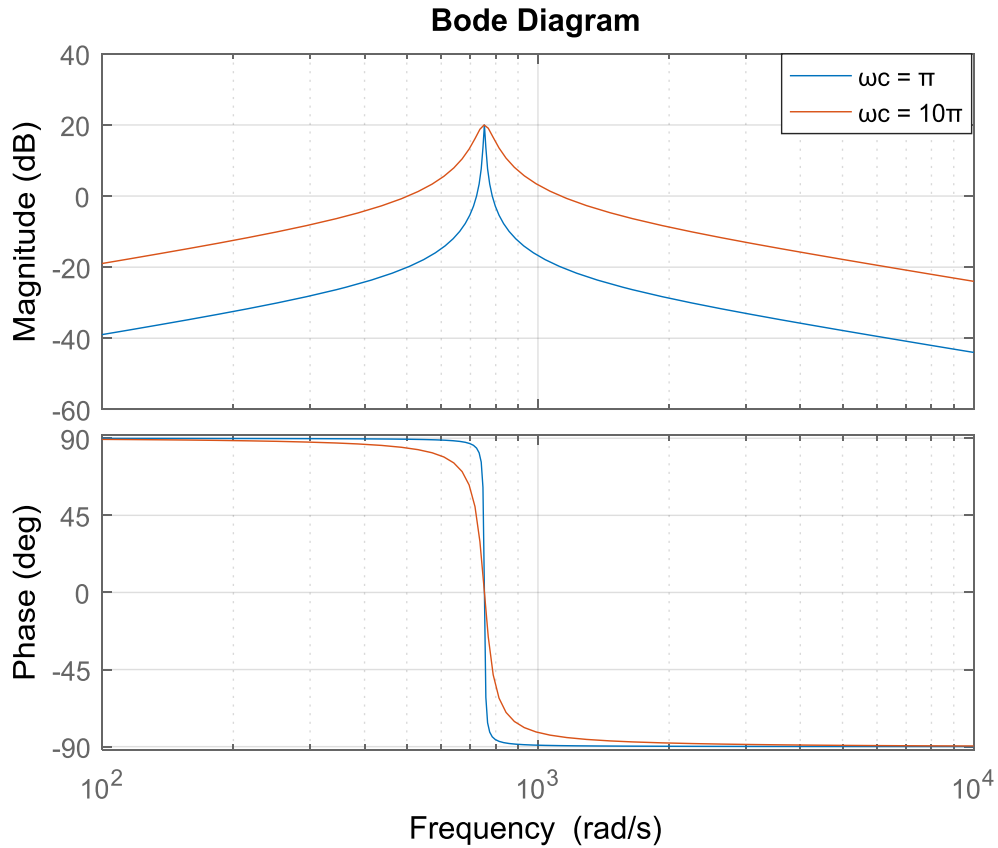


Figure 3.14: Frequency responses of a non-ideal PI+R controller when  $\omega_c$  changes.

### 3.3.2 Simulation results

The impact of the parameters of the PI+R controller on the attenuation of the low voltage ripple on the DC bus voltage will be investigated by means of simulations. The control system for the HESS, shown in Fig. 3.9, was modified by including the R part in the PI controller of the DC bus voltage loop, making it a PI+R controller. The controllers of the inner current loops remained the same as shown in Fig. 3.16. It should be noted that since the bandwidths of the current controllers are higher than that of the disturbance ( $2\pi 120$  rad/s), they should be able to produce a compensating current of the required magnitude. On the other hand, if the phase angle of the closed loop current controller is not zero at  $2\pi 120$  rad/s, which typically it is not, the disturbance should be mitigated but not completely eliminated.

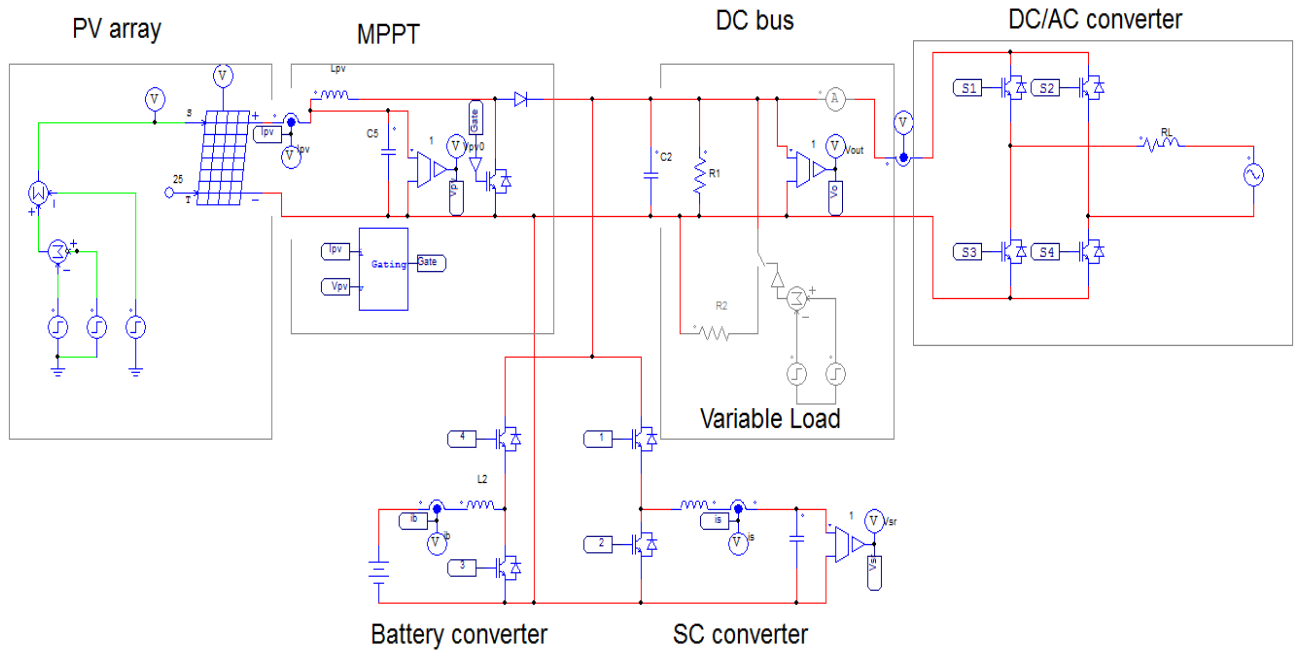


Figure 3.15: PV system and HESS with a single-phase dc/ac converter.

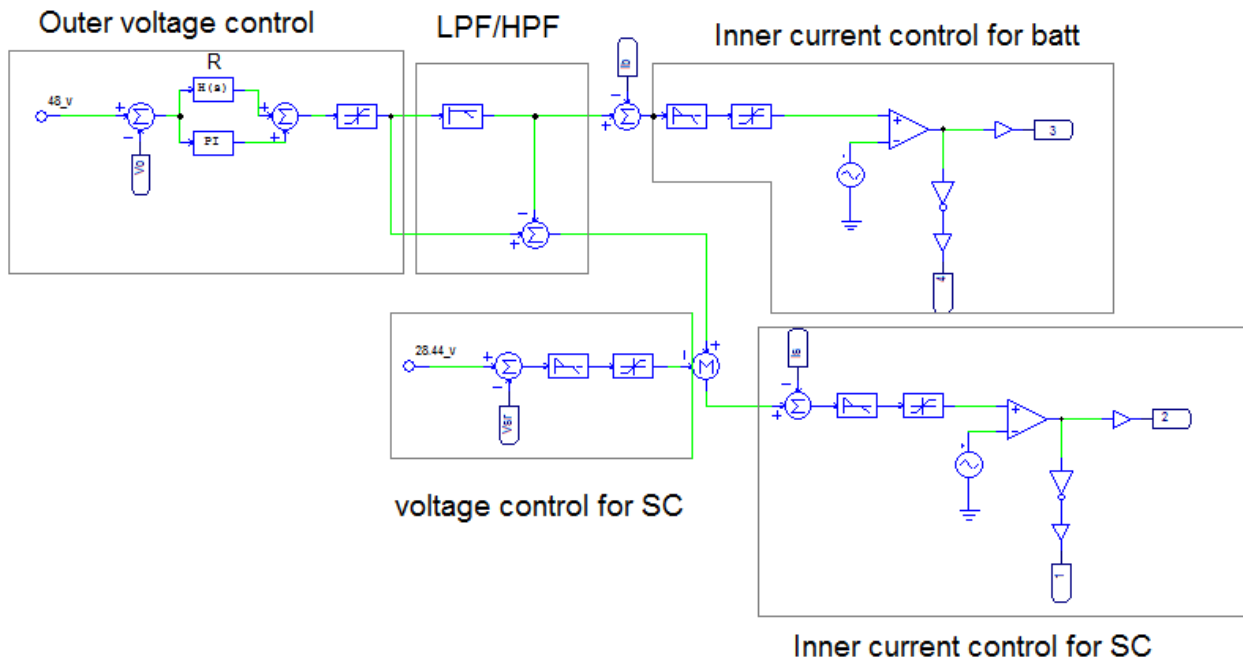


Figure 3.16: Control scheme of the HESS.

Fig. 3.17, shows the results of the system when a conventional PI controller is used for the DC bus voltage loop. A step load variation (40 to 20  $\Omega$ ) and AC current component with 120Hz are applied at  $t = 0.05$ s. Then, the load is restored to the initial value (40  $\Omega$ ) and the AC current component is disconnected. It can be observed, as shown in the waveforms, that a simple PI controller in the DC bus voltage loop is unable to significantly mitigate the ripple voltage produced by the 120 Hz current component. The gain of the PI controller at 120 Hz is relatively low, as observed in the small 120 Hz component on the battery and SC currents.

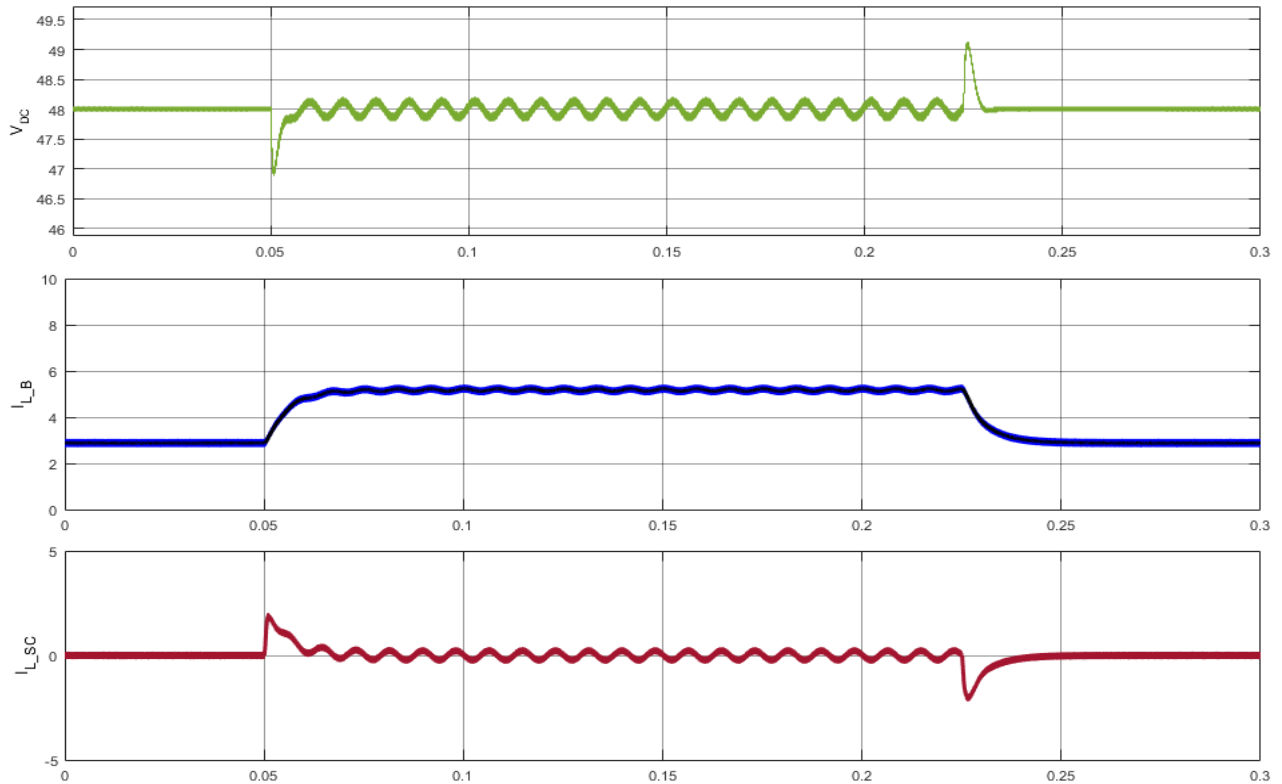


Figure 3.17: Waveforms for the system with PI Control: a) DC bus voltage; b) Battery current; c) SC current.

Fig. 3.18, shows the results of the system when the proposed PI+R controller is used in the DC bus voltage loop for the same test conditions described for Fig. 3.17. It can be observed, as shown in the waveforms, that by using the proposed PI+R controller in the DC bus voltage loop, the ripple in the DC bus voltage is significantly attenuated but a small oscillation appears at the moments of the step load variations.

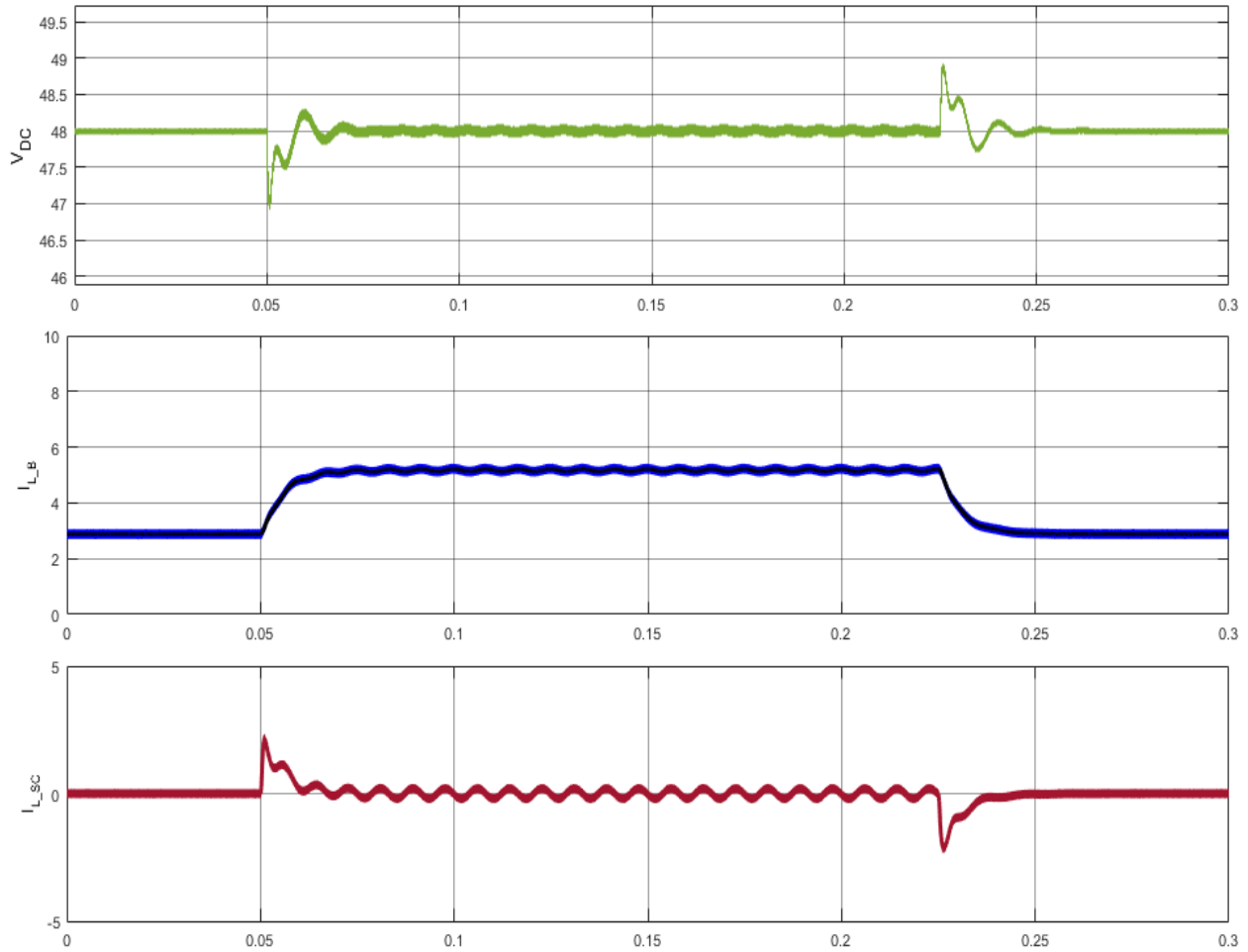


Figure 3.18: Waveforms for the system with PI+R Control: a) DC bus voltage; b) Battery current; c) SC current.

Fig. 3.19, shows the results of the system without the presence of the AC current component. A step load variation ( $40$  to  $20 \Omega$ ) is applied at  $t = 0.05\text{s}$ . Then, the load is restored to the initial value ( $40 \Omega$ ). It can be observed that by using the proposed PI+R controller in the DC bus voltage loop, the DC bus voltage is regulated at the desired value,  $48 \text{ V}$ , but a small oscillation appears at the moments of the step load variations. This will increase the time to regulate the DC bus voltage at the desired voltage  $48\text{V}$ .

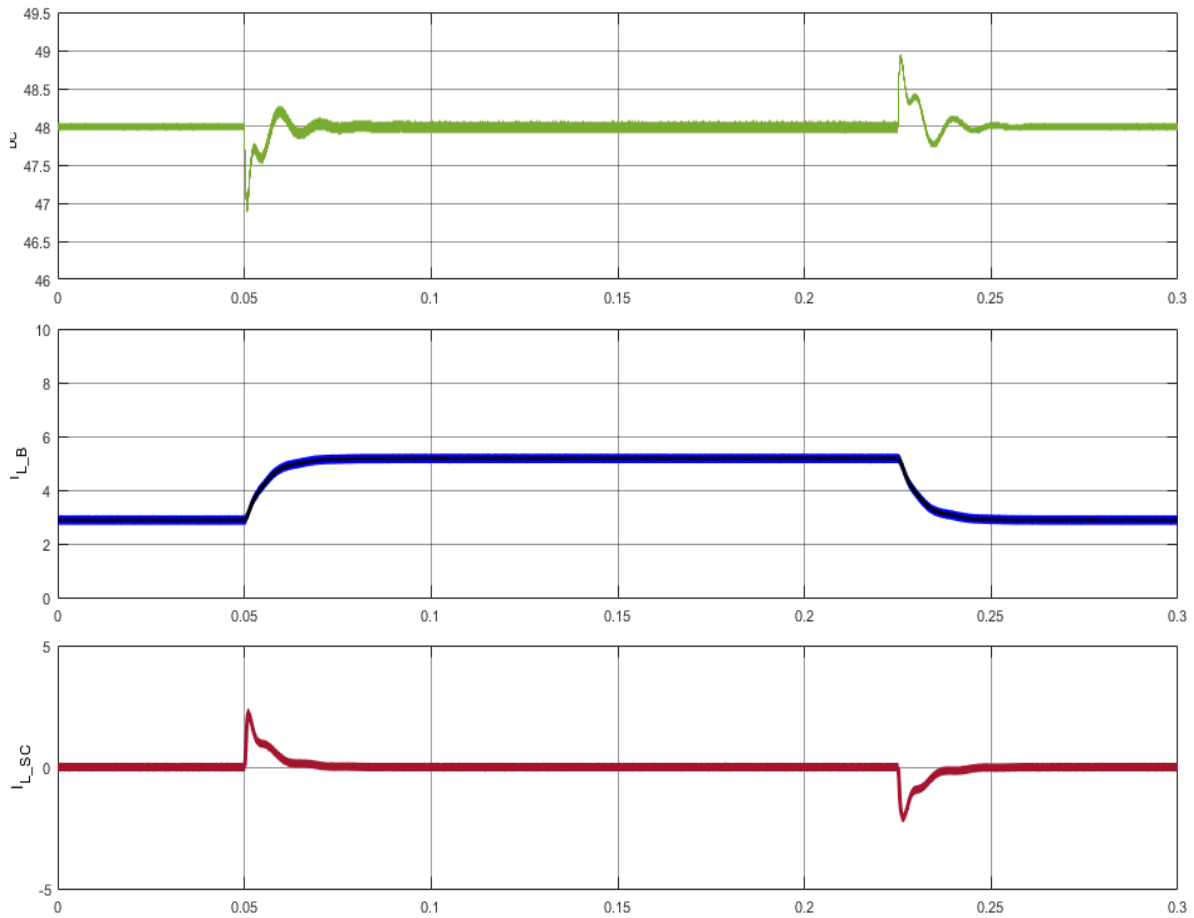


Figure 3.19: Waveforms for the system with PI+R Control: a) DC bus voltage; b) Battery current; c) SC current.

Finally, Fig. 3.20, shows the results of the system without the presence of the AC current component and with the standard PI type controller in the DC bus voltage regulation loop. A step load variation ( $40$  to  $20 \Omega$ ) is applied at  $t = 0.05$ s. Then, the load is restored to the initial value of  $40 \Omega$ . It can be observed that with a simple PI controller in the DC bus voltage loop no oscillations appear as when using the PI+R controller and it takes less time to regulate the voltage at  $48$  V.

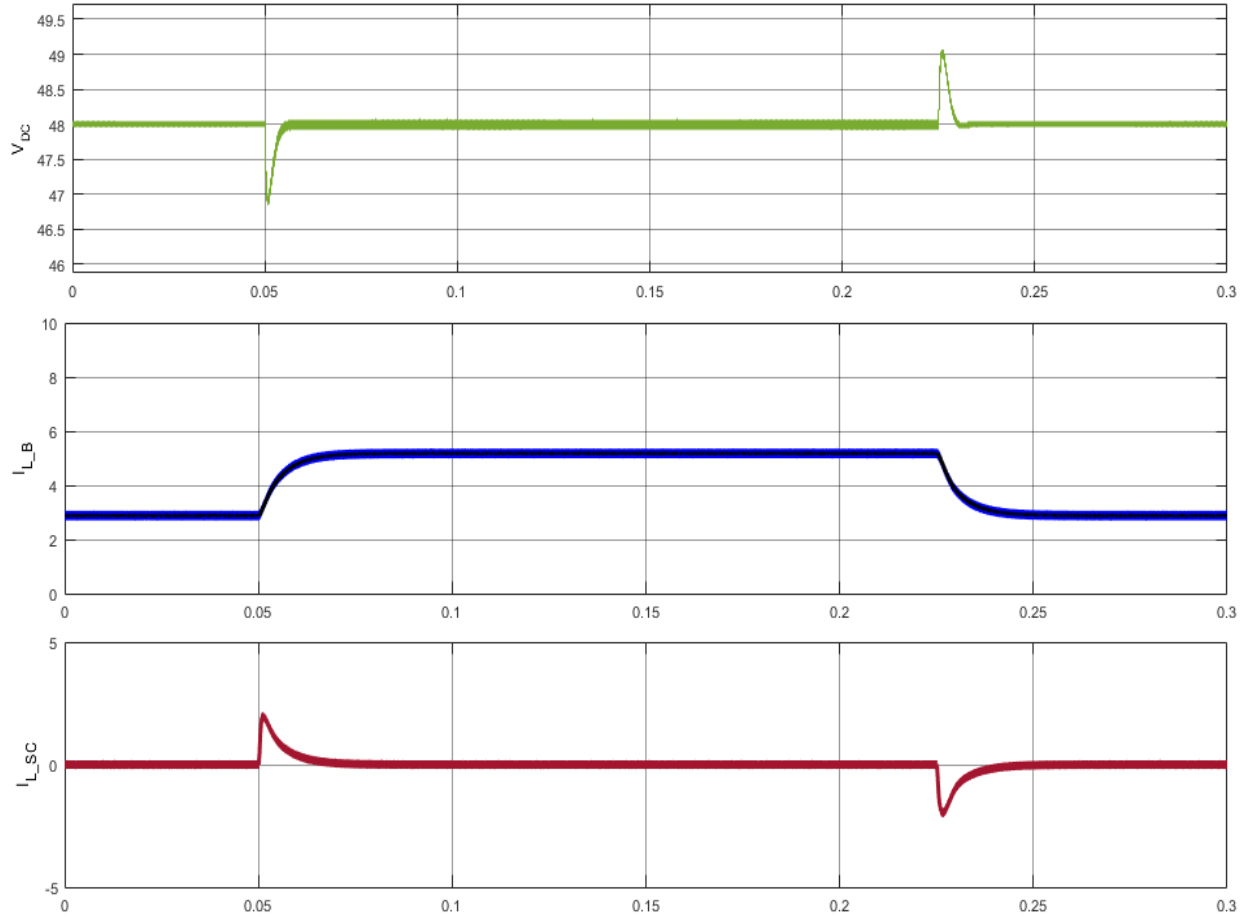


Figure 3.20: Waveforms for the system with PI Control: a) DC bus voltage; b) Battery current; c) SC current.

Overall, one can say that in the case of an AC current component, in the DC nano-grid, as a result of a single-phase inverter connected to an AC grid, by using a PI+R controller in the DC bus voltage loop, the ripple is significantly mitigated compared to the PI controller. However, if there are no active single-phase DC-AC converters connected to the DC bus, a small oscillation appears following transient step loads and the time to regulate the DC bus voltage at 48 V increases a bit compared to the system with a conventional PI. Since the benefits clearly outweigh the shortcomings, the use of a PI+R controller in the DC bus voltage controller is recommended.

### 3.4 Conclusion

This Chapter shows, first, the analysis and approach for selecting the crossover frequency of the HPF of a hybrid storage energy system (SC + Bat) which is required for splitting the reference current of the HESS into slow and fast components, for the battery and SC, respectively. It allows the determination of the amount of time the SC will contribute with the regulation of the DC bus voltage. For a longer contribution, more energy and a larger SC will be required. Simulation results were presented to validate the theoretical analysis and design approach. Second, the benefit of including a voltage loop for the SC. The performance of the system has been shown by testing it with and without the voltage control loop of the SC. Finally, a design of a proportional-integral plus resonant controller (PI+R) that is proposed for the DC bus voltage control loop to compensate for the low order harmonics in DC nano-grid introduced by a conventional single-phase DC-AC utility grid interface. Simulation results were presented to demonstrate that the proposed controller (PI+R) can mitigate the harmonics on the DC bus voltage better than the conventional PI controller.

## Chapter 4. Experimental Implementation

The primary goal in this Chapter is to implement the considered HESS control scheme for a standalone system and verify if it indeed is capable of regulating the DC bus voltage of a DC nano-grid, with varying power sources (PV) and loads. It is focused on the impact of the supercapacitor voltage, assuming it is not regulated in steady-state, on the dynamic response of the system. Besides, it considers the proposed approach for calculating the frequency of the LPF/HPF used for splitting the high frequency and low frequency components of  $I_{HESS}$ , so that the time of contribution of the SC is limited to a given value. The experimental setup for obtaining the results is described in this Chapter. The experimental results are presented and discussed for all the tests.

### 4.1 Experimental setup

An experimental prototype of a standalone PV system with HESS is implemented in this work. The realization of the considered control strategy is done by using dSPACE in real-time control. Data acquisition and the control system are implemented by using the dSPACE DS-1103 rapid prototyping system with a  $20\mu\text{s}$  time step. The dSPACE code is generated by Simulink C coder with execution of Real-time interface (RTI) that converts the control diagram from MATLAB/Simulink into dSPACE code. To build the DC-DC converters of the PV, battery and supercapacitor interfaces, the Semikron “MiniSKiiP 8 Three-phase 1200V Power board”, with a *MiniSKiiP 83 AC* power module and a *SKHI61* IGBT driver, is used. Each leg of the three-phase inverter is used for each DER. Two legs are used for battery and SC converters and they work as bidirectional while the last leg is used as the unidirectional interface of the RES as shown in Figure 4.1. The converters operate with pulse width modulation (PWM) and a switching frequency of 20 kHz. LC filters with values ( $100\mu\text{H}$  and  $470\mu\text{F}$ ) are used with each leg of the three-phase inverter to create the classical class C DC-DC converters. The capacitor across the DC bus voltage is  $1500\mu\text{F}$ . An Agilent Solar Array Simulator (SAS) (E4350B) was used to emulate a solar array. It was programmed to provide a maximum power of 213W with 7.35A and 29V at rated solar irradiance. Two Maxwell supercapacitor modules (BMOD0165 P048) with capacity of 165F and rated voltage of 48V are used for the energy storage units. One is used as a battery and the second is used as a SC. As mentioned in the nominal parameters for the SC and battery converters in Chapter 2, the “battery voltage” was adjusted to 24V and the SC’s to 28.44V. The inductor currents

of the battery and SC as well as the currents of load and PV are measured by LEM transducers (LA 55-P). The magnitudes of the voltages of the DC bus, battery, SC, and PV are measured by LEM transducers (LV 20-P). The resistive load bank used in the experiments consists of 8 parallel switchable resistors of  $40 \Omega$ . The Oscilloscope used to plot the waveforms of the results is a “YOKOGAWA SL1000”. The values of passive components and control parameters used in the experimental set-up are presented in *Chapter 2 “Section 2.4”*. The final implementation of the experimental set-up is shown in Figure 4.2.

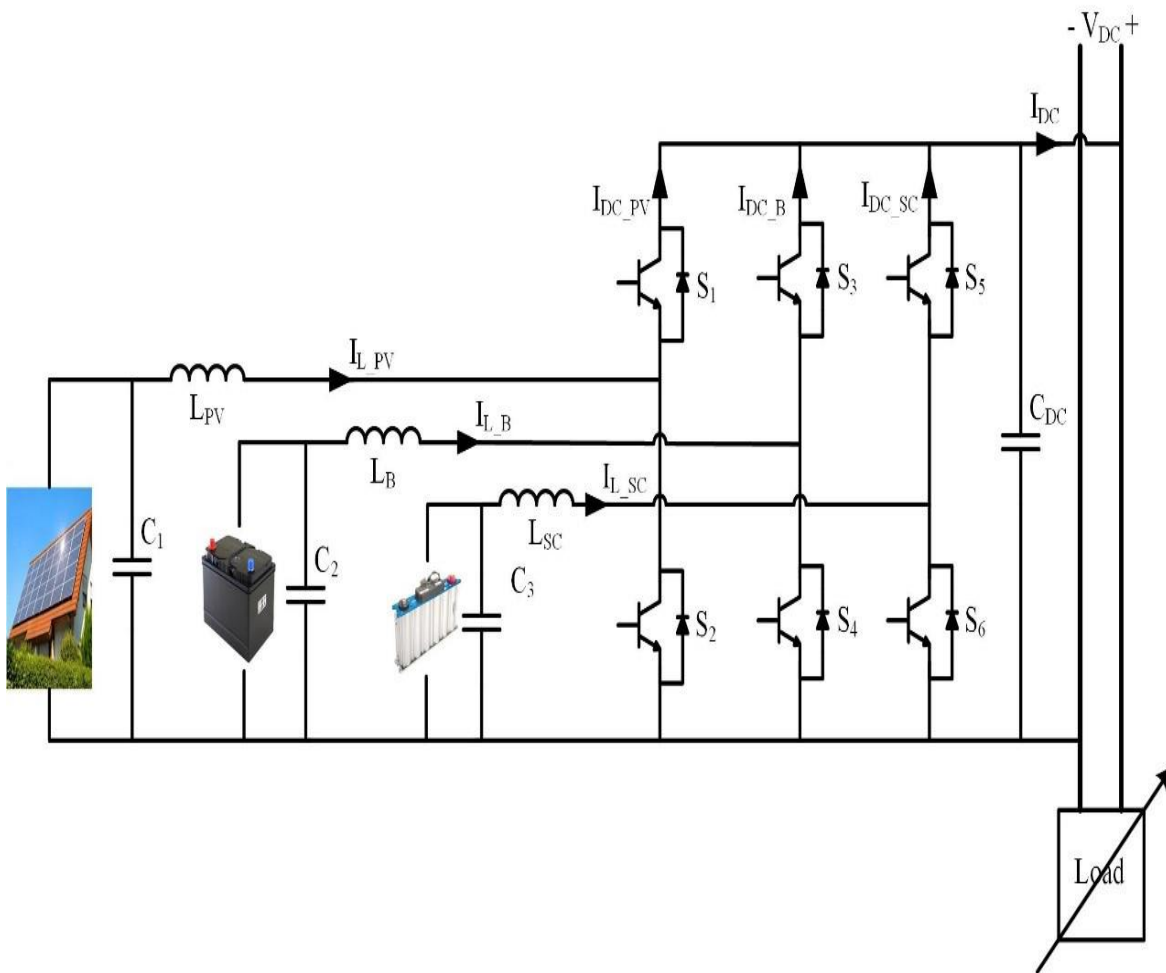


Figure 4.1: DC nano-grid power electronics interfaces.

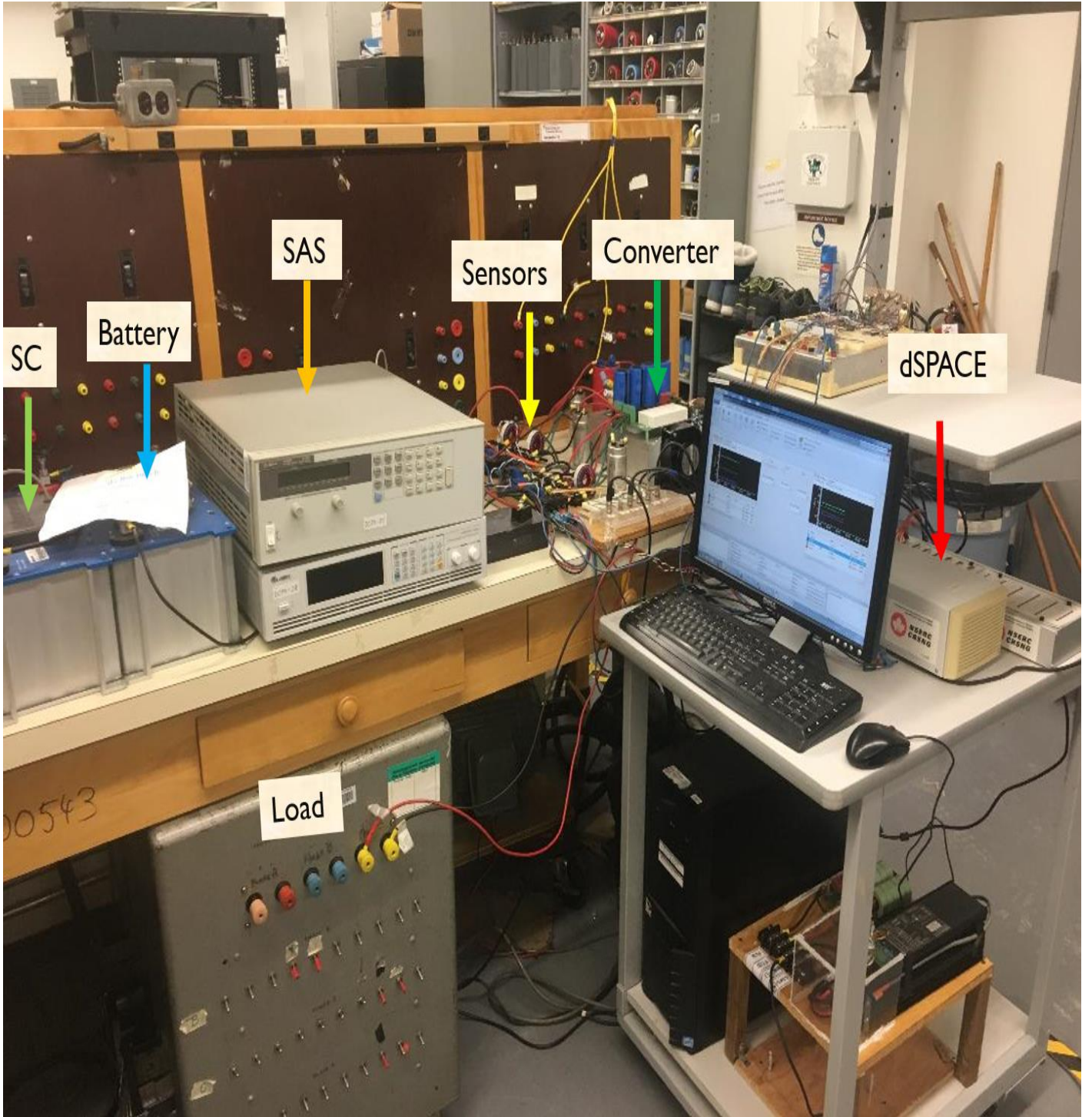


Figure 4.2: Picture of the experimental set-up assembled in the laboratory.

## 4.2 Experimental results

The objective is to demonstrate experimentally that the analytical equations and design approach work, as preliminarily shown by the simulations. In this Chapter, two experimental results were obtained. The first experiment result is to see the performance of the PI controllers, in terms of regulating the DC bus voltage, for the designed operating conditions, as well as others with low and high SC voltages. The second one is for the validation of the approach for calculating the cut-off frequency of the HPF, in order to obtain the SC providing current/support for the battery for a pre-determined period of time.

### 4.2.1 Results of the PI controller at different operating conditions

The performance of the PI controllers for operating conditions other than the designed one has been investigated by simulation in *Chapter 2*. This Section will present the validation of the performance of the PI controllers experimentally. In order to operate the PI controllers with different conditions, the voltage across the supercapacitor will be changed and consequently the value of the duty cycle of the main switch of the SC converter, what changes the values of the transfer function of the plant used in the design of the controllers.

The complete control system for the HESS that contains the DC bus voltage controller as well as the controllers of the inner current loops are designed for the supercapacitor working with an average voltage of 28.44V, leading to  $D = 0.4$ . Then, the results obtained from it will be compared with the same controller but by changing the duty cycle to  $D = 0.25, 0.75$  and this will be obtained by changing the voltage of the SC from 28.44V to 36 and 12V, respectively.

Figure 4.3, shows the experimental results of the system with  $V_{SC} = 28.44$  V and  $D = 0.4$ . It can be observed, as shown by the waveforms, that the system works as expected and the DC bus voltage is regulated at 48V and the battery and SC currents vary as expected. The SC current does not increase as fast as in the simulations, having a more roundish shape, but this should be due to the time/response delays of the microcontroller generating the gating signals to the SC converter as opposed to the one we get with the “instantaneous” response in the simulations.

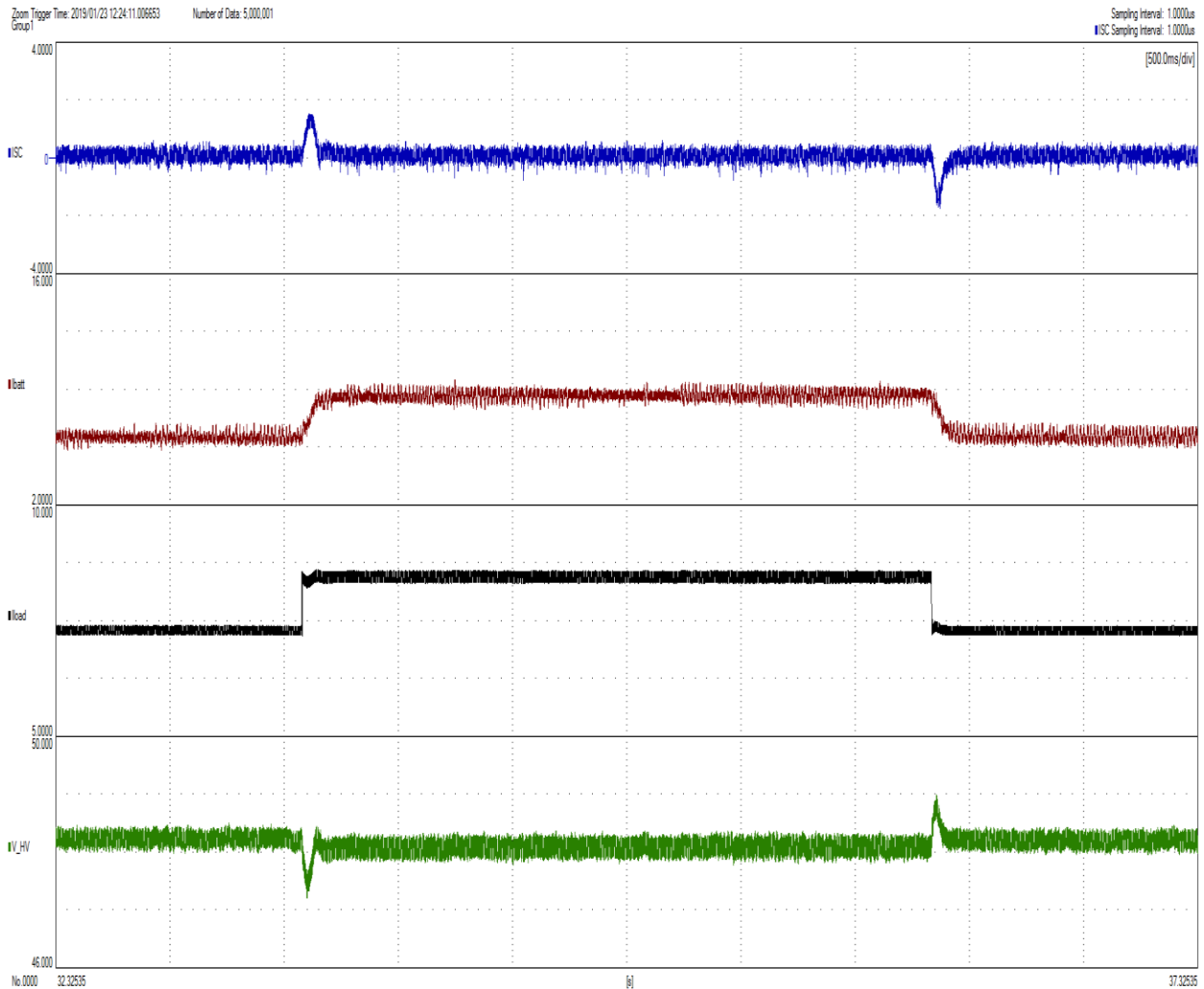


Figure 4.3: Waveforms for the system with a step load variation (9 to 6  $\Omega$ ): a) SC current; b) Battery current; c) Load current; d) DC bus voltage

Figure 4.4, shows the results of the system with  $V_{SC} = 36$  V and consequently  $D = 0.25$ . It can be observed as shown in the waveform that the system works well and that the DC bus voltage is regulated at 48V with less time and small overshoot than at  $D = 0.4$ . The battery and SC currents behave as expected.

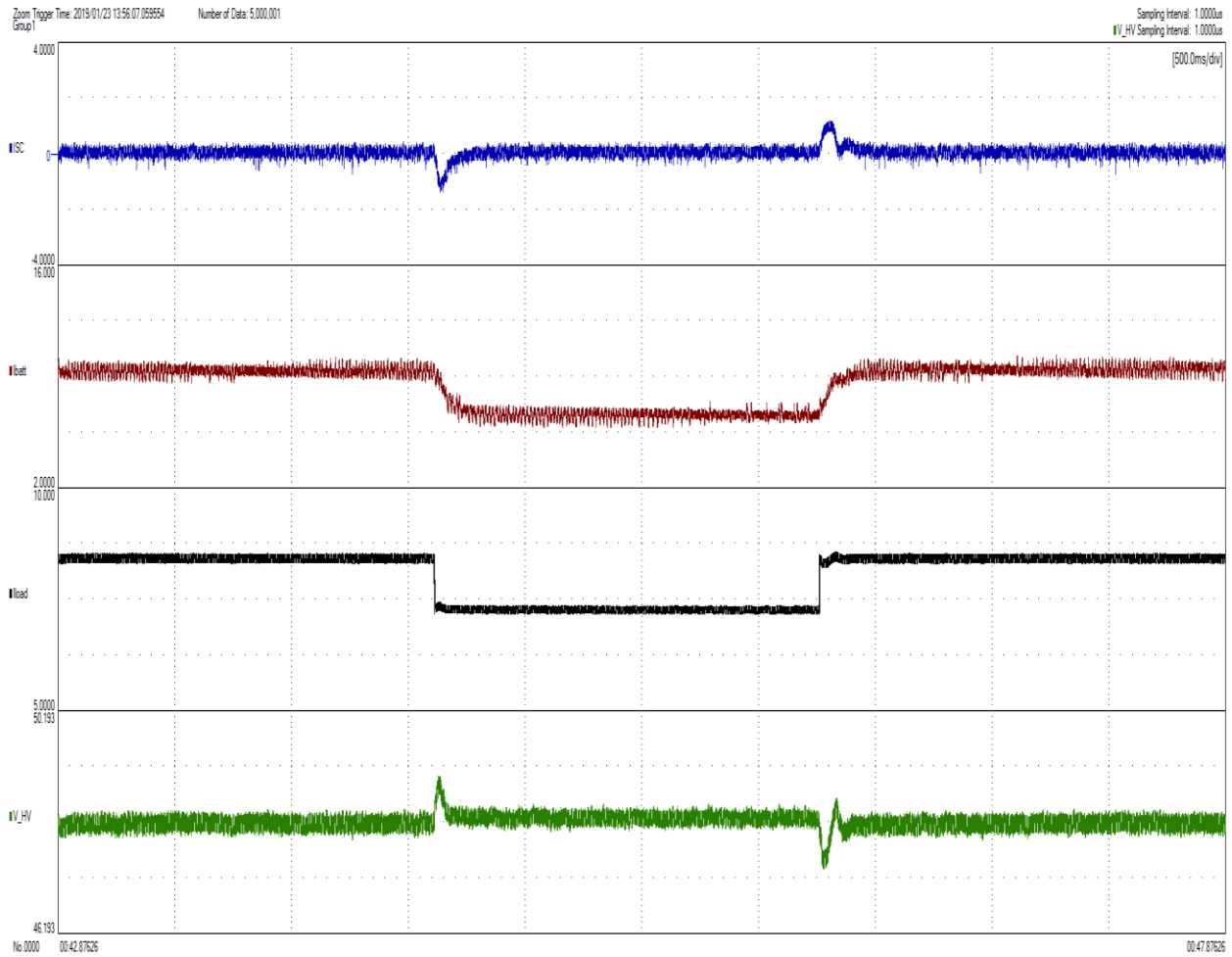


Figure 4.4: Waveforms for the system with a step load variation (9 to 6  $\Omega$ ): a) SC current; b) Battery current; c) Load current; d) DC bus voltage

Figure 4.5, shows the results of the system with  $V_{SC} = 12$  V and consequently  $D = 0.75$ . It can be observed, as shown in the waveforms, that a small oscillation on the DC bus voltage appears at the transient step as well as on the battery and SC currents.

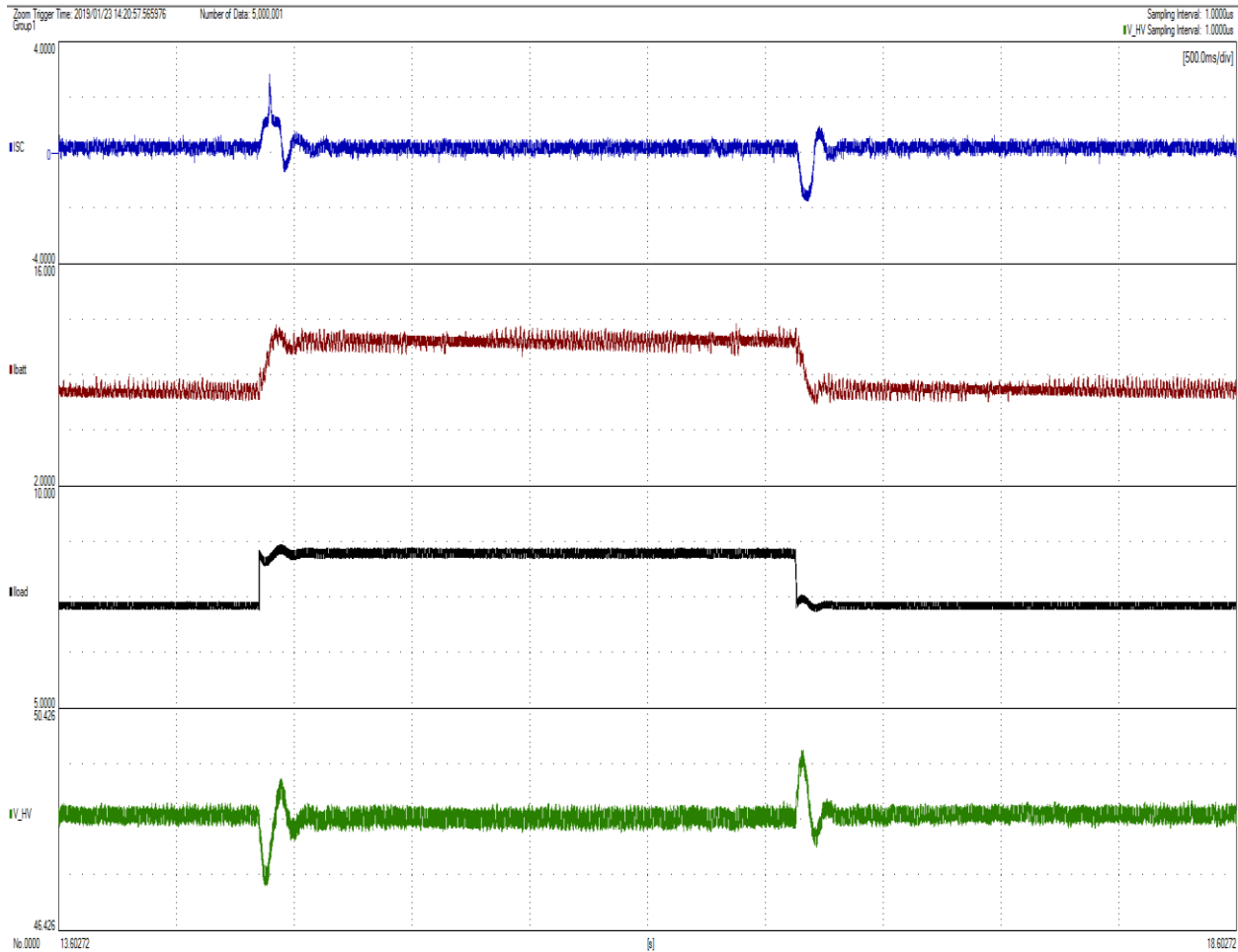


Figure 4.5: Waveforms for the system with a step load variation (9 to 6  $\Omega$ ) : a) SC current; b) Battery current; c) Load current; d) DC bus voltage

Overall, the results in all cases show that the DC bus voltage is regulated at 48V in steady-state. However, the effect of changing the voltage in the supercapacitor and consequently the duty cycle and transfer function of the plant is noticeable on the transient response. As shown in the results, a small oscillation on the DC bus voltage appears at the transient step in case of  $D = 0.75$  and this oscillation occurs because of the theoretical reduction in the PM to  $39.5^\circ$ . In the cases of  $D = 0.4, 0.25$  the PM =  $60^\circ, 62.3^\circ$  respectively the system works with the expected transient response. For comparison purposes, the simulation results of a similar system is presented in *Chapter 2* “*Section 2.6*”, where one can see that the experimental results are very similar to those of the simulation.

#### 4.2.2 Results concerning the choice of the HPF (frequency) of a HESS.

The main objective of this Section is to observe the reaction of the DC bus voltage as well as the currents of the SC and battery as one changes the cut-off frequency of the HPF, what should lead to the times ( $T$ ) stated in Table 3.1.

Considering the HESS control scheme that was shown in Fig. 2.2, *Chapter 2*, the experimental results will be obtained with the parameters that have been presented in *Chapter 2* for the voltage control loop and the current control loops, as well as their converter parameters.

Figure 4.6, shows the experimental results of the system with the cut-off frequency of the LPF at  $f = 0.37\text{Hz}$  for a step load variation (20 to 13  $\Omega$ ). One can see that the current contribution of the SC drops to 10% of the final value 5A, i.e. 0.5 A, at  $t \sim 1\text{ s}$ , as well as the battery current reaches 90% of the final value as expected based on Table 3.1.

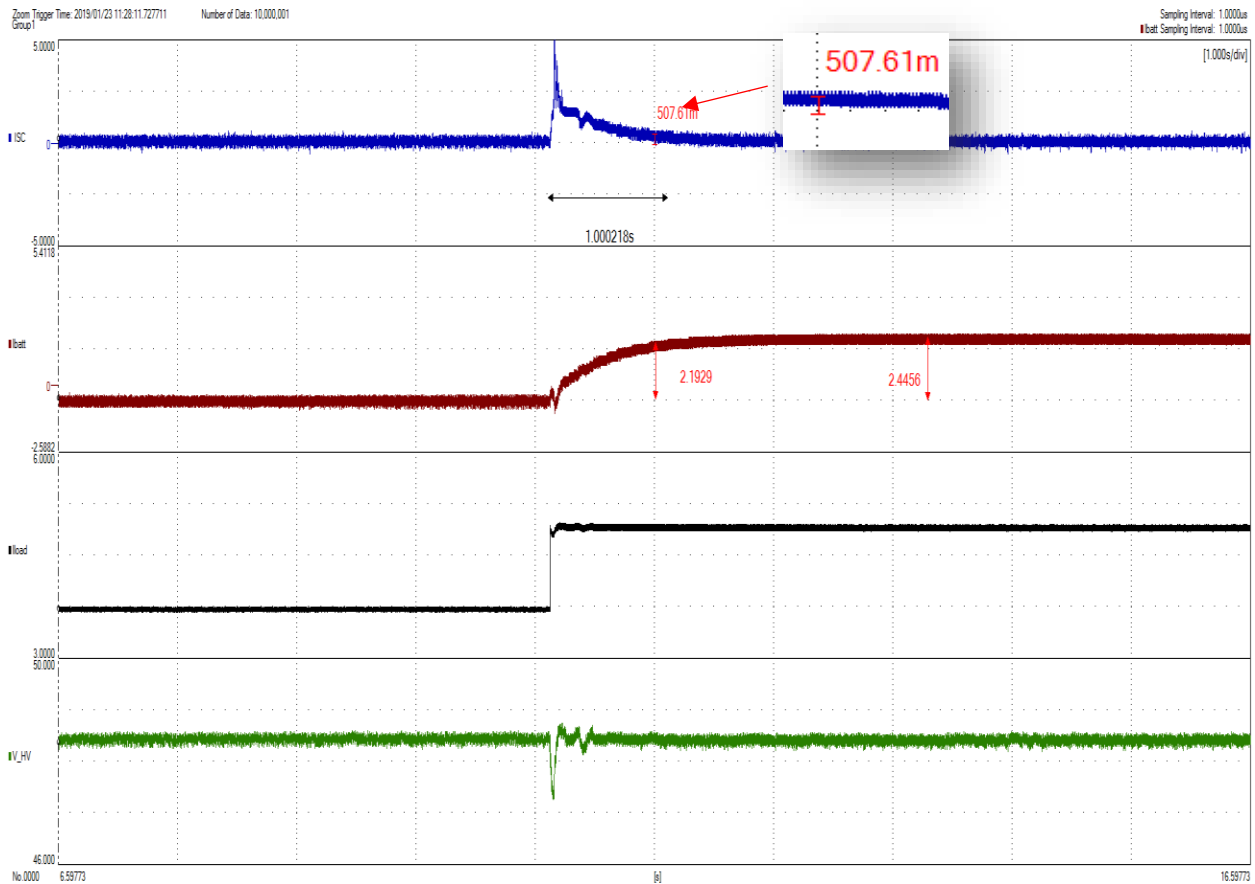


Figure 4.6: Waveforms for the system with  $f = 0.37\text{Hz}$  for a step load variation (20 to 13  $\Omega$ ): a) SC current; b) Battery current; c) Load current; d) DC bus voltage.

Figure 4.7, shows the experiment results of the system with the cut-off frequency of the LPF at  $f = 0.037\text{Hz}$  for a step load variation ( $20$  to  $13 \Omega$ ). One can see that the current contribution of the SC drops to 10% of the final value  $5\text{A}$ , i.e.  $0.5 \text{A}$ , at  $t \sim 10 \text{s}$ , as well as the battery current reaches 90% of the final value as expected.

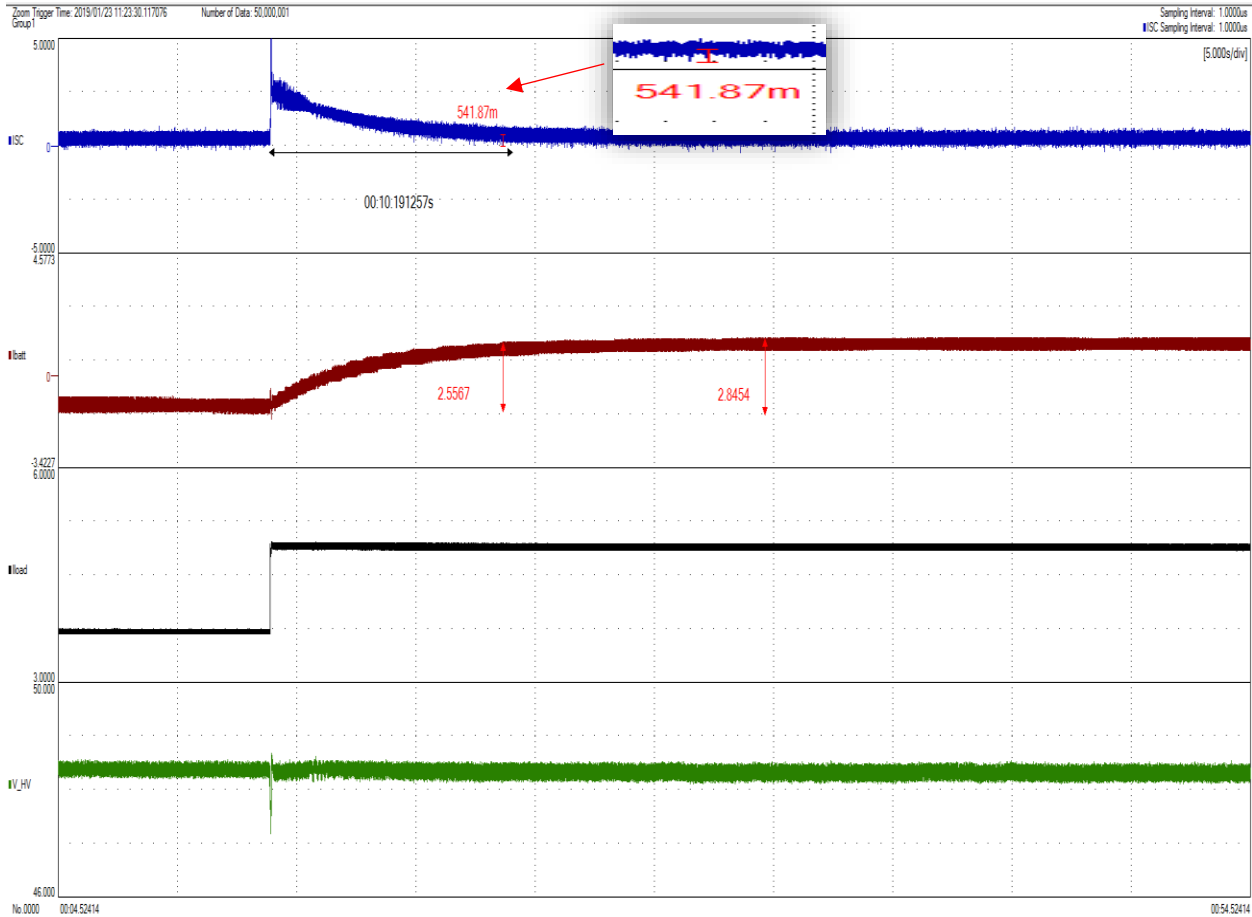


Figure 4.7: Waveforms for the system with  $f = 0.037\text{Hz}$  for a step load variation ( $20$  to  $13 \Omega$ ): a) SC current; b) Battery current; c) Load current; d) DC bus voltage.

Figure 4.8, shows the experiment results of the system with the cut-off frequency of the LPF at  $f = 0.0037\text{Hz}$  for a step load variation ( $20$  to  $13 \Omega$ ). One can see that the current contribution of the SC drops to 10% of the final value  $5\text{A}$ , i.e.  $0.5 \text{A}$ , at  $t \sim 100\text{s}$ , as well as the battery current reaches 90% of the final value as expected.

*Note that 1:40:039s that is shown in the waveforms means 1 minute and 40 seconds which is 100seconds.*

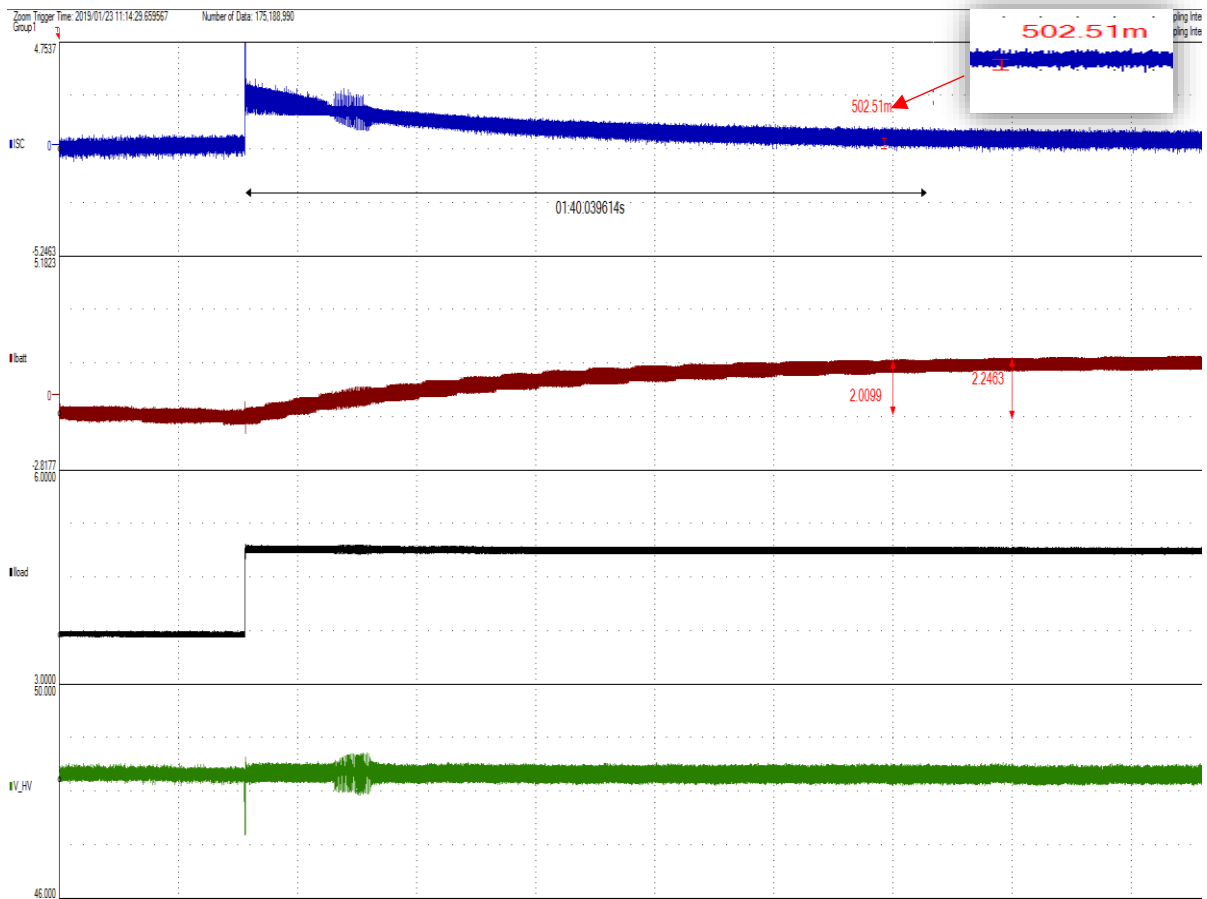


Figure 4.8: Waveforms for the system with  $f = 0.0037\text{Hz}$  for a step load variation (20 to 13  $\Omega$ ): a) SC current; b) Battery current; c) Load current; d) DC bus voltage.

### 4.3 Conclusion

In this Chapter, the implementation of a DC nano-grid connecting a hybrid energy storage system (HESS) with a PV system to supply power to a DC load is presented. The experimental results for verifying the performance of the cascaded control scheme, outer voltage and inner currents, with PI type controllers were presented and it is validated the theoretical analysis and simulation results. The experimental validation of the approach for calculating the cut-off frequency of the HPF in order to obtain the SC providing current/support for the battery for a pre-determined period of time was presented as well.

## Chapter 5. Conclusions and Future Work

The system considered in this Thesis is a PV converter supplying a DC bus with MPPT and having a hybrid energy storage system (HESS) to balance power supply and load demand thus regulating the DC bus voltage. In order to connect the battery and supercapacitor (SC) of the HESS with the PV system to supply power to a DC load class C DC-DC converters are used for the interfaces. So, power flow can be controlled in both directions by controlling the current in the battery and supercapacitor. Therefore, the control scheme of the HESS is based on a single outer voltage loop with two inner current loops, for the inductors of the battery and SC. A low pass filter is used to split the fast (transient) and the slow (steady-state) components of the reference current obtained from the outer voltage loop, and send them to the SC and battery current loops, respectively. Three PI controllers have been designed to control the (inner) current through the SC and the battery as well as the outer DC bus voltage. The bandwidth of these controllers are chosen based on the speed of response of each single converter, which is a function of its switching frequency and type of storage medium.

To see the performance of the PI controllers for operating with different conditions, the voltage across the supercapacitor was changed and consequently the value of the duty cycle of the main switch of the SC converter, what changes the values of the transfer function of the plant used in the design of the controllers. This should lead to a variation in the dynamic response of the system, which becomes more oscillatory as the voltage in the SC decreases. The experimental results for performance of PI controller were presented and it is validated the theoretical analysis and simulation results. In principle, by including a SC voltage control loop, presented in Section 3.2, one should prevent this issue. In this work, the selected reference value was the one that allows the SC to supply, before reaching 50% of rated voltage, and absorbing the amount of energy, before reaching 100% of rated voltage.

As mentioned earlier, the main objective of the control strategy is to allow the supercapacitor (SC) to support the fast transients and the battery bank to provide the slow transient and steady-state current components so as to get good static and dynamic regulation of the DC bus voltage while reducing the stress on the battery. For that, it is important to develop an approach to determine the frequency of the LPF that splits the total compensating current of the HESS in reference for the SC and battery converters. This would be based on how long (ms, s or minute)

the SC converter keeps injecting/adsorbing current for a given step load/power variation event. The validation of the approach for calculating the cut-off frequency and the energy supplied/absorbed by the SC was done by means of simulation as well as experimentally.

A DC nano-grid can also be connected to an AC utility through interface converters, what is performed by a DC-AC converter or inverter. The single-phase DC-AC grid interface converter provides bidirectional power flow, but it draws/injects a DC component as well as an AC current component, leading to a voltage ripple of twice the AC side fundamental frequency. Usually, a large electrolytic capacitor is used to filter the voltage ripple and provide a pure DC voltage. However, this capacitor has a large and a short life. In order for a smaller non-electrolytic capacitor to be used, some sort of active power filtering needs to be done, what can be done by means of the HESS with a suitable control scheme. Therefore, the HESS control has been modified by adding a resonant element at the frequency of the disturbance to the PI controller, making it a PI+R. With a high gain in the DC bus voltage loop at the frequency of the disturbance, it was possible to achieve a significant reduction in the voltage of the DC nano-grid as shown by means of simulation results.

As future work, the following is suggested:

- 1) Conduct the experimental verification with the PI+R DC bus voltage controller in an AC utility grid connected DC nano-grid.
- 2) Introduce a logic in the control of the HESS so that the battery will not further discharge if its State-of-Charge (SoC) is low, or charge if the SOC is high, preventing it from premature aging.
- 3) Investigate the case where the PV converter and the HESS are not in close proximity. In such a case, the impedance between the converters should lead to a voltage error in the DC bus voltage.

## References

- [1] S. K. Kollimalla, M. Mishra and N. Narasamma, "Design and analysis of novel control strategy for battery and supercapacitor storage system," *IEEE Transactions on Sustainable Energy*, vol. 5, no. 4, pp. 1137-1144, Oct. 2014.
- [2] U. Manandhar, N. R. Tummuru, S. K. Kollimalla, A. Ukil and G. H. Beng, "Validation of Faster Joint Control Strategy for Battery- and Supercapacitor-Based Energy Storage System," *IEEE Transactions on Industrial Electronics*, vol. 65, no. 4, pp. 3286 - 3295, 2018.
- [3] S. Kolluri and N. L. Narasamma, "Analysis, modeling, design and implementation of average current mode control for interleaved boost converter," *2013 IEEE 10th International Conference on Power Electronics and Drive Systems (PEDS)*, vol. 5, pp. 280-285, 2013.
- [4] M. G. Molina, "Control design and simulation of supercapacitor energy storage for microgrid applications," in *2014 IEEE PES Transmission & Distribution Conference and Exposition - Latin America (PES T&D-LA)*, Medellin, Colombia, 2014.
- [5] F. Chen, R. Burgos and D. Boroyevich, "Efficiency comparison of a single-phase grid-interface bidirectional AC/DC converter for DC distribution systems," in *2015 IEEE Energy Conversion Congress and Exposition (ECCE)*, Montreal, QC, Canada, 2015.
- [6] F. Chen, R. Burgos, D. Boroyevich and X. Zhang, "Low-Frequency Common-Mode Voltage Control for Systems Interconnected With Power Converters," *IEEE Transactions on Industrial Electronics*, vol. 64, no. 1, pp. 873 - 882, 2017.
- [7] A. Etxebarria, I. Vechiu, H. Camblong and J. Vinassa, "Comparison of three topologies and controls of a hybrid energy storage system for microgrids," *Energy Conversion and Management*, vol. 51, no. 1, pp. 113-121, 2012.
- [8] H. Cha, T.-K. Vu and J.-E. Kim, "Design and control of Proportional-Resonant controller based Photovoltaic power conditioning system," in *2009 IEEE Energy Conversion Congress and Exposition*, San Jose, CA, USA, 2009.
- [9] N. Mendis, K. M. Muttaqi and S. Perera, "Active power management of a super capacitor-battery hybrid energy storage system for standalone operation of DFIG based wind turbines," in *2012 IEEE Industry Applications Society Annual Meeting*, Las Vegas, NV, USA, 2012.
- [10] M. Glavin, P. K. Chan, S. Armstrong and W. Hurley, "A stand-alone photovoltaic supercapacitor battery hybrid energy storage system," *2008 13th International Power Electronics and Motion Control Conference*, vol. 8, pp. 1688-1695, 2008.
- [11] D. B. W. Abeywardana and B. Hredzak, "Supercapacitor Sizing Method for Energy-Controlled Filter-Based Hybrid Energy Storage Systems," *IEEE Transactions on Power Electronics*, vol. 32, no. 2, pp. 1626-1637, 2017.

- [12] M. C. Joshi and S. Samanta, "Average current mode control of battery/ultracapacitor hybrid energy system & its microcontroller based implementation," in *2018 IEEMA Engineer Infinite Conference (eTechNxT)*, New Delhi, India, 2018.
- [13] U. Manandhar, A. Ukil, S. K. Kollimalla and H. B. Gooi, "Application of HESS for PV system with modified control strategy," in *2015 IEEE Innovative Smart Grid Technologies - Asia (ISGT ASIA)*, Bangkok, Thailand, 2015.
- [14] J. Cao and A. Emadi, "A New Battery/UltraCapacitor Hybrid Energy Storage System for Electric, Hybrid, and Plug-In Hybrid Electric Vehicles," *IEEE Transactions on Power Electronics*, vol. 27, no. 1, pp. 122 - 132, 2012.
- [15] Y. Zhang, Z. Jiang and X. Yu, "Control Strategies for Battery/Supercapacitor Hybrid Energy Storage Systems," in *2008 IEEE Energy 2030 Conference*, Atlanta, GA, USA, 2009.
- [16] M. Hamzeh, A. Ghazanfari, Y. A.-R. I. Mohamed and Y. Karimi, "Modeling and Design of an Oscillatory Current-Sharing Control Strategy in DC Microgrids," *IEEE Transactions on Industrial Electronics*, vol. 62, no. 11, pp. 6647 - 6657, 2015.
- [17] Q. Xu, J. Xiao, P. Wang, X. Pan, and C. Wen, "A decentralized control strategy for autonomous transient power sharing and state-of-charge recovery in hybrid energy storage systems," *IEEE Trans. Sustain. Energy*, vol. PP, no. 99, pp. 1, 2017, doi: 10.1109/TSTE.2017.2688391.
- [18] N. Femia, G. Petrone, G. Spagnuolo and M. Vitelli, "A Technique for Improving P&O MPPT Performances of Double-Stage Grid-Connected Photovoltaic Systems," *IEEE Transactions on Industrial Electronics*, vol. 56, no. 11, pp. 4473 - 4482, 2009.
- [19] S. Dusmez and A. Khaligh, "A supervisory power-splitting approach for a new ultracapacitor, battery vehicle deploying two propulsion machines," *IEEE Trans. Ind. Informat.*, vol. 10, no. 3, pp. 1960–1971, Aug. 2014.
- [20] S. Jeyasudha and B. Geethalakshmi, "Modeling and control of integrated photovoltaic module and converter systems," in *2017 Innovations in Power and Advanced Computing Technologies (i-PACT)*, Vellore, India, 2018.
- [21] H. Fakham, D. Lu and B. Francois, "Power Control Design of a Battery Charger in a Hybrid Active PV Generator for Load-Following Applications," *IEEE Transactions on Industrial Electronics*, vol. 51, no. 1, pp. 85 - 94, 2011.
- [22] S. M. Cherati, N. A. Azli, S. M. Ayob and A. Mortezaei, "Design of a current mode PI controller for a single-phase PWM inverter," in *2011 IEEE Applied Power Electronics Colloquium (IAPEC)*, Johor Bahru, Malaysia, 2011.
- [23] F. Chen, R. Burgos, D. Boroyevich and X. Zhang, "Active control of low frequency common mode voltage to connect AC utility and 380 V DC grid," in *2016 IEEE Applied Power Electronics Conference and Exposition (APEC)*, Long Beach, CA, USA, 2016.

- [24] F. Chen, R. Burgos, D. Boroyevich and D. Dong, "Control loop design of a two-stage bidirectional AC/DC converter for renewable energy systems," in *2014 IEEE Applied Power Electronics Conference and Exposition - APEC 2014*, Fort Worth, TX, USA, 2014.
- [25] Y.-c. Zhang, L.-l. Wu, X.-j. Zhu and H.-q. Liang, "Design of supercapacitor-based energy storage system for metro vehicles and its control rapid implementation," in *2008 IEEE Vehicle Power and Propulsion Conference*, Harbin, China, 2008.
- [26] B. Hredzak, V. G. Agelidis, and M. Jang, "A model predictive control system for a hybrid battery-ultracapacitor power source," *IEEE Trans. Power Electron.*, vol. 29, no. 3, pp. 1469–1479, Mar. 2014.
- [27] H. El Fadil, F. Giri, J.M. Guerrero, and A. Tahri, "Modeling and nonlinear control of a fuel cell/supercapacitor hybrid energy storage system for electric vehicles," *IEEE Trans. Veh. Technol.*, vol. 63, no. 7, pp. 3011–3018, Sep. 2014.
- [28] A. Lahyani, P. Venet, A. Guermazi, and A. Troudi, "Battery/ Supercapacitors combination in uninterruptible power supply (UPS)," *IEEE Trans. Power Electron.*, vol. 28, no. 4, pp. 1509 - 1522, 2013.
- [29] X. Feng, H. B. Gooi, and S. X. Chen, "Hybrid energy storage with multimode fuzzy power allocator for PV systems," *IEEE Trans. Sustain. Energy*, vol. 5, no. 2, pp. 389 - 397, 2014.